THE ASTROPHYSICAL JOURNAL, 469:147–165, 1996 September 20

THE X-RAY SPECTRAL VARIABILITY OF MARKARIAN 766

KAREN M. LEIGHLY[1]
Cosmic Radiation Laboratory, RIKEN, Hirowasa 2–1, Wakoshi, Saitama 351, Japan
RICHARD F. MUSHOTZKY AND TAHIR YAQOOB[2]
Code 662.0, NASA Goddard Space Flight Center, Greenbelt, MD 20771
HIDEYO KUNIEDA
Department of Physics, Nagoya University, Furo-cho, Chikusa-ku, Nagoya 464, Japan
AND
RICK EDELSON
Department of Physics and Astronomy, University of Iowa, Iowa City, IA 52242-1479
Received 1995 August 30; accepted 1996 March 14

ABSTRACT

Analysis results from *ASCA* and *ROSAT* observations of the narrow-line Seyfert 1 galaxy Mrk 766 are reported. In the *ASCA* observation, we observed rapid variability with a doubling timescale of 1000 s. A spectral variability event was observed in which the spectrum softened and hardened above and below ~ 1 keV, respectively, as the flux increased. The spectra could be modeled with five components: an absorbed power law, warm absorber, iron Kα line, and soft excess component flux. The spectral variability resulted from a highly significant change in the intrinsic photon index from $\Gamma \sim 1.6$ to ~ 2.0, an increase in the warm absorber ionization, and a marginally significant decrease in the soft component normalization. A ~ 100 eV equivalent width narrow iron Kα line was detected in the high-state spectrum. Spectral hardening during flux increases was observed in three *ROSAT* observations.

The change in intrinsic photon index and disappearance of the soft excess component in the *ASCA* spectra can be explained as a transition from a first-order pair-reprocessed spectrum to a pair cascade brought about by a sudden increase in the injected electron Lorentz factor. The change in the ionization of the warm absorber, though model dependent, could correspond to the increase in flux at the oxygen edges resulting from the spectral index change. The *ROSAT* spectral variability can be interpreted by variable intensity hard power law and a relatively nonvarying soft component, possibly primary disk emission. These results are compared with those reported from other narrow-line Seyfert 1 galaxies.

Subject headings: galaxies: individual (Markarian 766) — galaxies: Seyfert — radiation mechanisms: nonthermal — X-rays: galaxies

1. INTRODUCTION

Mrk 766 is a bright ($F_{(2-10)} \sim 2 \times 10^{-11}$ ergs cm^{-2} s^{-1}), soft ($\Gamma_{0.1-2.4} \sim 2.7$) X-ray source at redshift $z = 0.012$. The spectrum measured with the *Einstein* IPC and MPC was complex and ultrasoft ($\Gamma = 1.77$; $kT = 18.6$ eV; Urry *et al.* 1990). A shortest timescale of variability of 1000 s and a steep and variable power-law index was found in a long observation using *EXOSAT* (Molendi, Maccacaro, & Schaeidt 1993). During the *ROSAT* All Sky Survey, Mrk 766 was bright ($F_{0.1-2.4} \sim 1.5 \times 10^{-10}$ ergs cm^{-2} s^{-1} [unabsorbed]), and variability by a factor of 3 with no accompanying spectral variability was observed in 10–12 hr (Molendi et al. 1993). Pointed *ROSAT* observations revealed spectral variability that Netzer, Turner, & George (1994) showed could not be explained by a change in ionization of a warm absorber and that Molendi & Maccacaro (1994) attributed to a change in the accretion rate.

Mrk 766 is a member of the X-ray narrow-line Seyfert 1 (NLS1) galaxy class (Osterbrock & Pogge 1985; Goodrich 1989). *ROSAT* observations of NLS1s find soft 0.1–2.4 keV X-ray spectra and rapid, large-amplitude soft X-ray variability. The soft X-ray spectra of NLS1s are systematically steeper than the spectra of broadline Seyfert 1 galaxies (Boller, Brandt, & Fink 1996 and references therein). A harder high-energy power-law component generally was not observed in the relatively soft *ROSAT* band. Only a few observations at higher energies have been reported. The *ASCA* spectrum of the NLS1 object IRAS 13224−3809 is dominated below ~ 2 keV by a soft excess and from 2 to 10 keV by a hard ($\Gamma \sim 1.3$) power law (Otani 1995). In contrast, a very steep spectrum with $\Gamma_{(2-10\ \mathrm{keV})} \sim 2.6$ was found from the NLS1 object RE 1034+39 (Pounds, Done, & Osborne 1995).

We report the results from 1993 December *ROSAT* and *ASCA* observations of Mrk 766. Timing analyses of two *ROSAT* archival observations are also presented. In § 2, the data reduction is discussed briefly. In § 3, timing analyses using normalized variability amplitudes and hardness ratios are presented. In § 4, the spectral analysis of the *ASCA* data is described. The results are discussed in terms of standard models in § 5 and are compared with reported results from other NLS1s. A summary and conclusions are given in § 6.

2. *ASCA* AND *ROSAT* OBSERVATIONS OF MARKARIAN 766

We observed Mrk 766 with *ASCA* and the *ROSAT* PSPC during 1993 December. It had been previously observed with the *ROSAT* PSPC several times. Two longer observations were made on 1991 June 15 and 1992 December 21, and these data were extracted from the *ROSAT* archive. The observation log is given in Table 1.

The data were reduced using Xselect. To ensure that all soft photons were collected, *ROSAT* extraction regions of 3′

[1] Previously an NRC fellow at NASA Goddard Space Flight Center.
[2] Also Universities Space Research Association.

TABLE 1

OBSERVING LOG

Instrument (1)	Observation Date (2)	Exposure (s) (3)	Total Counts[a] (4)	Background Count Rate[b] (5)
ROSAT PSPC.....	1991 Jun 15	15179[c]	21804	0.081
ROSAT PSPC.....	1992 Dec 21	16303[d]	53865	0.056
ROSAT PSPC.....	1993 Dec 17	3146	7309	0.033
ASCA S0	1993 Dec 18	32947	32823	0.030
ASCA S1	1993 Dec 18	32735	26853	0.020
ASCA G2	1993 Dec 18	35805	16991	0.033
ASCA G3	1993 Dec 18	35808	19532	0.032

[a] Total (not background subtracted) counts in the source extraction region.
[b] Background rate scaled to the source extraction region.
[c] Exposure time after data selection to remove periods where the source was occulted by a rib.
[d] Exposure time in the first 85,000 s of observation. The total observation time was 19,870 s.

for the on-axis 1993 observation and 4′ for the off-axis 1991 and 1992 observations were used. Extraction of background subtracted light curves from the events files was done using IDL software. The light curves from the off-axis 1991 and 1992 observations were corrected for vignetting. In the 1991 observation, Mrk 766 was periodically occulted by the detector rib, so time periods in which the flux dropped to zero because of occultation were excluded (see, e.g., Brandt et al. 1993). A region of the same radius located diametrically across the detector and subjected to the same good time interval selection provided an approximately correctly normalized background.

ASCA data were reduced using standard selection and cleaning criteria. Background for the GIS was obtained from a source-free region in the GIS field of view approximately the same distance from the optical axis as the source. Background SIS spectra were obtained from blank sky fields, while background count rates for the light curves were determined from the edges of the SIS chips. The time-dependent gain shift in the SIS was accounted for by filling and using PI columns. Spectra were extracted using Xselect, and background-subtracted light curves were obtained from the cleaned events files using IDL.

Figure 1*a* shows the *ROSAT* PSPC and *ASCA* SIS0 light curves from the most recent, quasi-simultaneous 1993 observations. Error bars represent 1 σ statistical error. The *ROSAT* observation started $\sim$20,000 s before the *ASCA* observation but was unfortunately cut short as the satellite went into safe hold mode. The *ROSAT* PSPC light curves from the 1991 and 1992 observations are shown in Figure 1*b*. Mrk 766 was brightest in the *ROSAT* band in 1992 at <5 counts s^{-1}. This is comparable to the flux level observed during the *ROSAT* All Sky Survey observation (Molendi et al. 1993). In order to make a direct comparison with the other data, only the first $\sim$80 ks of the 1992 observation were considered. The remainder consists of data from only two orbits and is separated from the main part of the observation by nearly 1 day, and the full light curve is shown in Netzer et al. (1994).

3. TIMING ANALYSIS

3.1. *Fastest Observed Variability*

The *ASCA* light curves were examined in order to find instances of rapid variability that could be clearly identified in all four detectors. A dip in flux occurred at $\sim$50,000 s from the start of the observation; the light curve from the SIS0 detector is shown embedded in Figure 1*a*. At the end of the dip, the flux increased by nearly a factor of 2 in $\sim$1000 s. This timescale is the same order as those observed in *ASCA* data from other Seyfert 1 nuclei, including NGC 4051 ($\Delta t \sim 200$ s; Mihara et al. 1994).

Assuming that the X-ray emission originates from a single region, the minimum flux-doubling timescale Δt gives an upper limit on the source size as $R \sim c\Delta t$ of 3×10^{13} cm, where c is the speed of light. This estimate breaks down if the X-rays are emitted from many small regions.

Because of the telescope wobble, variability on timescales less than 400s generally cannot be detected in *ROSAT* data. Significant variability was observed consistently between adjacent orbits ($\Delta t \sim 6000$ s). The fastest variability of the three observations was found when it was brightest during the 1992 observation. A 30% increase in 2400 s occurred 3400 s from the beginning of the observation (Fig. 1*b*).

3.2. *Variance Analysis*

The normalized variability amplitude (NVA), defined to be the standard deviation divided by the mean intensity, provides a simple way to quantify the variability in different energy bands (see, e.g., Edelson 1992). If the width of the energy band is chosen so that the number of photons in each light curve is the same, the NVA collapses to the square root of the variance.

The *ASCA* light curves from each detector were accumulated with 100 s binning in the 4–10 keV band where the power-law component should dominate the spectrum. The light curves were not background subtracted. However, the dilution of the variability by the constant background was small, since the background rate in the highest energy band where contribution is largest was only, e.g., $\sim$8% of the SIS0 count rate. The data below 4 keV were divided into energy bands with bounds chosen so that the light curves had the same mean square measurement error $\sigma_{\rm err}^2$ as in the 4–10 keV band. Note that each resulting band was wider than the energy resolution at that band. The true variance of the data given by $\sigma_{\rm int}^2 = \sigma_{\rm obs}^2 - \sigma_{\rm err}^2$ is plotted as a function of energy in Figure 2. The 1 σ uncertainties in the variance are less than 10% of the values (eq. [2] of Done et al. 1992). These variance plots demonstrate that the variability amplitude over the whole observation is smallest at hard energies, peaks near 1 keV, and decreases toward lower energies in the SISs.

For the *ROSAT* light curves, three standard energy bands were considered: the "*a* band" (channels 11–41, energy 0.1–0.4 keV), the "*c* band" (channels 52–90, energy

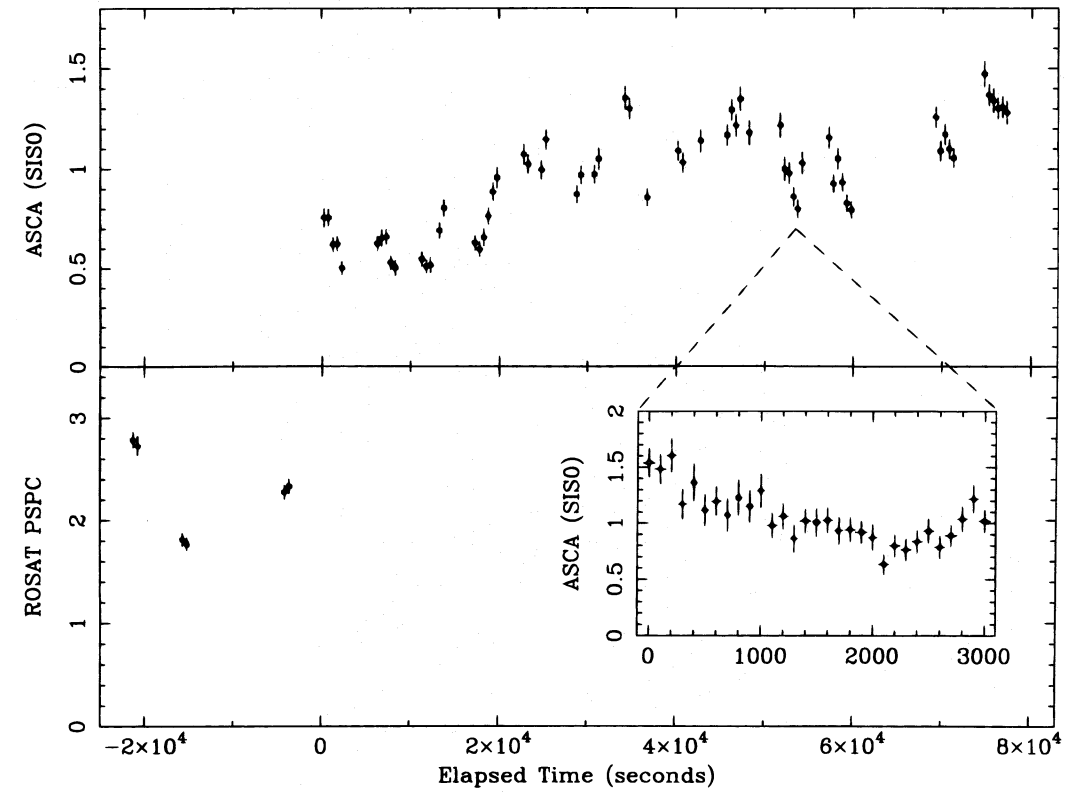

FIG. 1*a*

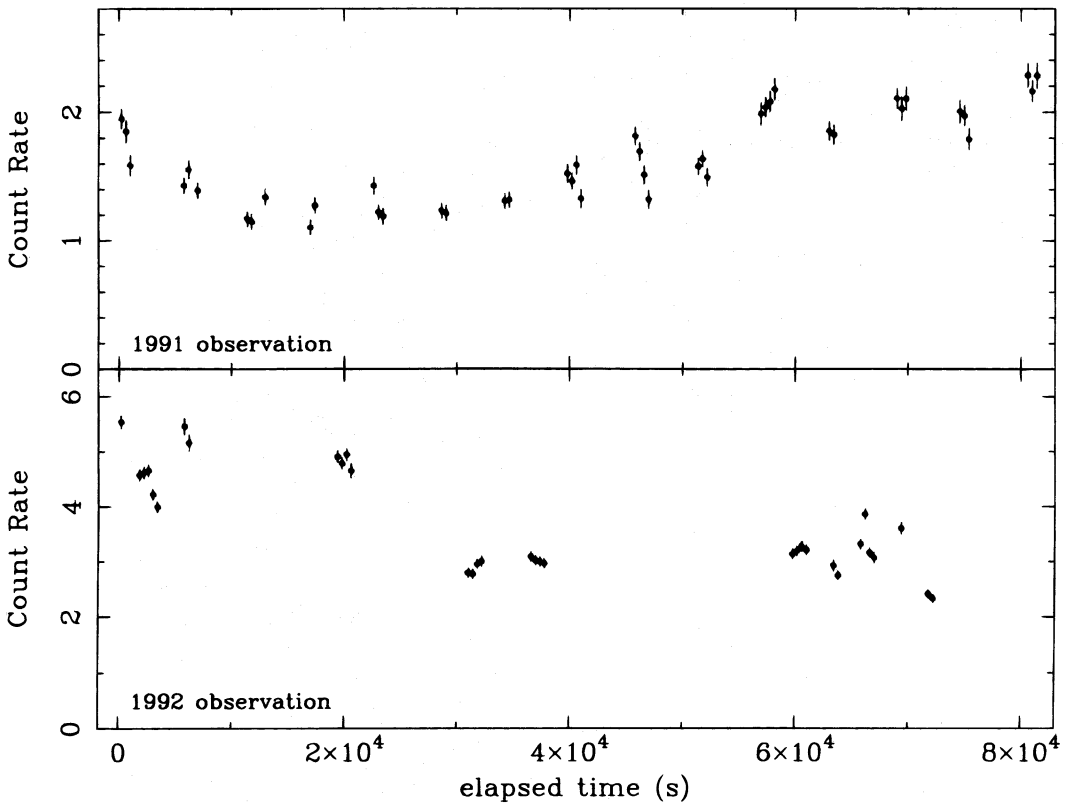

FIG. 1*b*

FIG. 1.—(*a*) The 1993 *ROSAT* PSPC (0.1–2 keV) and *ASCA* SIS0 (0.4–10 keV) light curves with the same absolute timescale. The *ASCA* data were binned by good time intervals with minimum interval of 300 s. The binning for the *ROSAT* light curves is 400 s to account for the wobble of the telescope. The SIS0 light curve from the period of most rapid variability is embedded. (*b*) The 1991 and 1992 *ROSAT* PSPC (0.1–2 keV) light curves corrected for vignetting and on the same relative timescale.

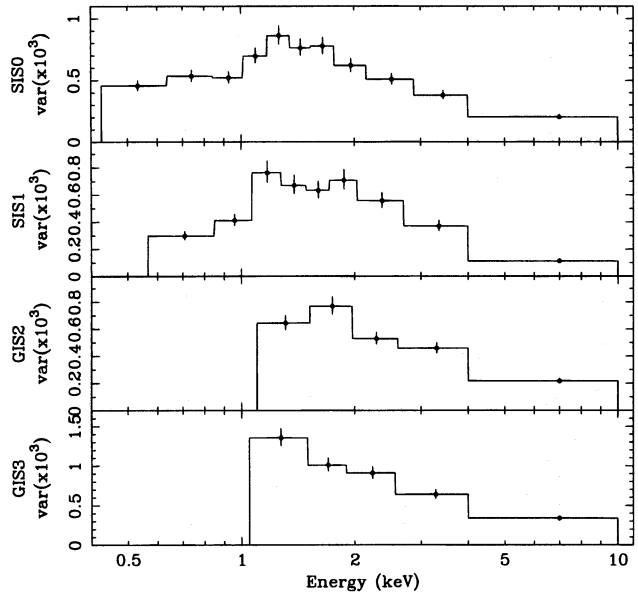

FIG. 2.—Variance vs. energy of *ASCA* light curves for each detector in energy bands with bounds chosen so that the mean square measurement error $\sigma_{\rm err}^2$ is the same in each. These show that the largest variability amplitude occurred at ~1 keV.

0.5–0.9 keV), and the "*d* band" (channels 91–201, energy 0.9–2 keV). These bands are independent and roughly correspond to regions in which different spectral features will dominate: the soft excess in the *a* band, the warm absorber in the *c* band, and the power law in the *d* band. The binning of the background-subtracted light curves was chosen to be 400 s to account for the telescope wobble.

Because of the rib occultations in the 1991 data, it was necessary to include data with net exposure per bin of 200–400 s, even though the shorter exposure bins add noise to the light curve. The light curves in these three bands are shown on the left in Figures 3*a*, 3*b*, and 3*c*. Mrk 766 is bright enough and the bin size is long enough that the signal-to-noise ratio (S/N) is better than 6 in all bins. Variability was detected in each energy band, and the χ^2 values for a constant hypothesis model fit and the computed NVAs are listed in Table 2. The NVAs show that in all observations, the source is significantly less variable in the lowest energy band compared with the higher energy bands.

TABLE 2

PSPC VARIABILITY

Band	Mean	χ_ν^2	NVA
1991 Data (44 points):			
Total.....	1.35	17.6	0.22
0.2–0.5.....	0.84	6.0	0.16
0.5–0.9.....	0.20	7.05	0.36
0.9–2.0.....	0.22	8.54	0.37
1992 Data (41 points):			
Total.....	3.06	77.5	0.26
0.2–0.5.....	1.63	22.7	0.19
0.5–0.9.....	0.58	24.9	0.34
0.9–2.0.....	0.67	35.1	0.38
Quasi-simultaneous Data (eight points):			
Total.....	2.24	29.9	0.19
0.2–0.5.....	1.33	8.2	0.13
0.5–0.9.....	0.39	13.9	0.31
0.9–2.0.....	0.39	13.6	0.31

3.3. *Flux Ratios*

The hardness ratio (4.0–10.5 keV/1.0–1.35 keV) and softness ratio (0.4–0.7 keV/1.0–1.35 keV) light curves from the *ASCA* SIS0 detector are shown in Figures 4*a* and 4*b*, respectively. Following Ptak et al. (1994), the values were computed using variable bin sizes corresponding to good time intervals longer than 300 s. A large decrease in hardness corresponding to a softening of the spectrum was observed in the hardness ratio light curve at about 20,000 s from the beginning of the observation (Fig. 4*a*). The light curves show that the spectral change is due to a large increase in 1.0–1.35 keV flux, while the 4–10 keV flux remained nearly constant. Significant variability in the softness ratio was also observed at the same time, such that the spectrum below 1 keV hardens when the flux increases (Fig. 4*b*). The hardening of the spectrum may be more gradual, and it is not clearly completed until after ~25,000 s. Variability was observed in both energy bands, but the amplitude is larger in the 1.0–1.35 keV band. The spectral variability is confined to the region around 20,000 s elapsed time. Other instances of large-amplitude flux variability occurred (e.g., at ~35,000 s) with no corresponding spectral change. Thus, the spectral variability is not strictly correlated with the flux.

ROSAT softness ratio light curves (0.1–0.4 keV/0.9–2.0 keV and 0.5–0.9 keV/0.9–2.0 keV) are shown on the right-hand sides of Figures 3*a*, 3*b*, and 3*c*. Spectral variability is most pronounced between the hardest and softest bands, with the spectrum generally hardening as the flux increased. This result is also true from observation to observation; the spectrum was hardest when the source was brightest in 1992 and softest when it was dimmest in 1991. On long timescales, the softest band varies proportionately less than the harder bands. On short timescales, the spectral variability is not correlated with the flux. At high flux, when the source was most rapidly variable, correlated variability occurred with no change in the hardness ratio (1992: at the beginning of the observation). Similar correlated variability was observed during the *ROSAT* All Sky Survey when the source was also quite bright (Molendi et al. 1993). In contrast, at low flux in the 1991 and 1992 observations, orbit-to-orbit deviations in the hardest band occurred that were not followed in the softest band (1991: at ~23,000 and ~58,000 s; 1992: at ~66,000 s). These short-timescale hard band excursions result in dips in the softness ratio.

4. SPECTRAL ANALYSIS

Based on the softness and hardness ratios, the *ASCA* data were divided in two as shown in Figures 4*a* and 4*b*, and spectra were accumulated avoiding the transition region between ~15,000 and ~25,000 s from the beginning of the observation. These spectra are referred to as the low-state and high-state spectra and represent exposures of ~8000 and 20,000 s, respectively. Figure 5 shows the pulse-height analyzer channel ratios from the low state divided by the high state of the summed SIS0 and SIS1 spectra in the top panel and of the summed GIS2 and GIS3 spectra in the bottom panel. These confirm the results of the variance analysis, which were that the spectrum is most variable at around 1 keV, the variability amplitude decreases to lower and higher energies, and the flux is essentially constant at

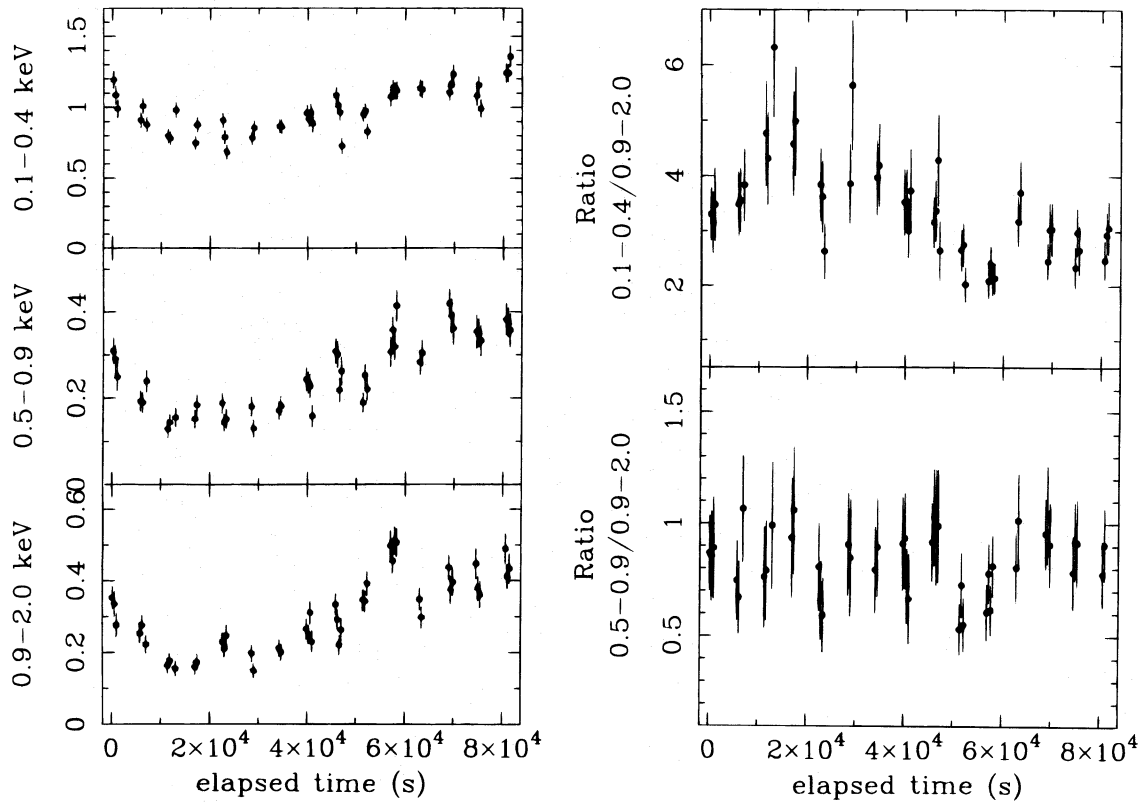

FIG. 3*a*

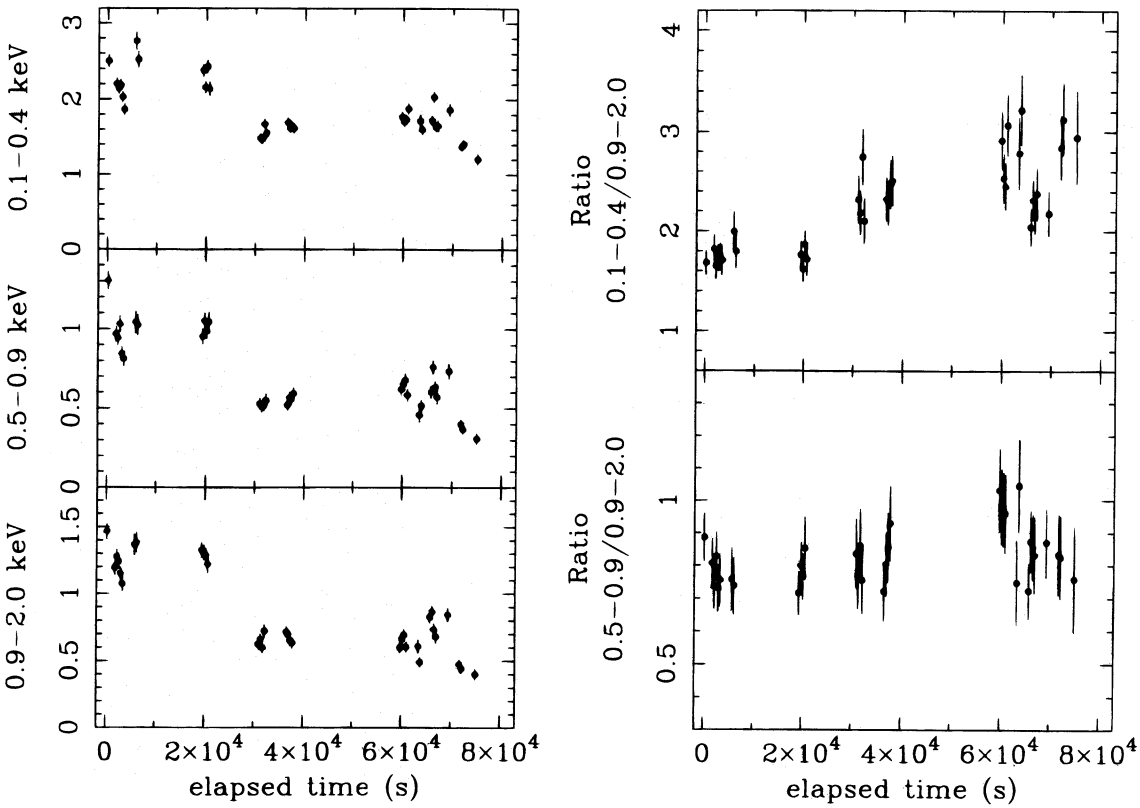

FIG. 3*b*

FIG. 3.—On the left, vignetting-corrected *ROSAT* light curves in three standard energy bands, and on the right, the softness ratio light curves. The time bin size was 200–400 s. (*a*) 1991 observation; (*b*) 1992 observation; (*c*) 1993 observation.

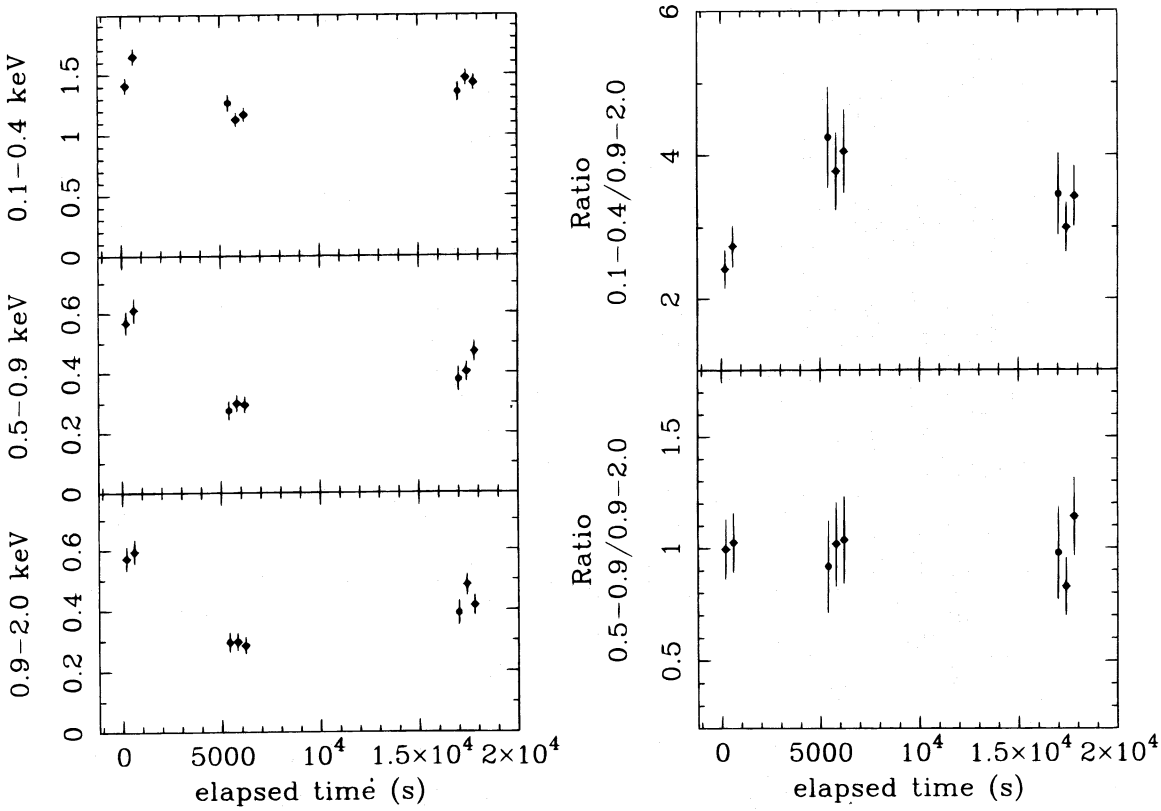

FIG. 3c

about 10 keV.

4.1. *The Hard X-Ray Spectrum*

An estimation of the power-law index, assuming that any warm absorber does not have a large column density, was obtained by fitting the four spectra above 2 keV with a power-law plus iron Kα line model. The low- and high-state spectral indices were 1.57 ± 0.07 and $2.00^{+0.03}_{-0.04}$, respectively, and the results from fitting each detector separately were consistent. Throughout this paper, quoted uncer-

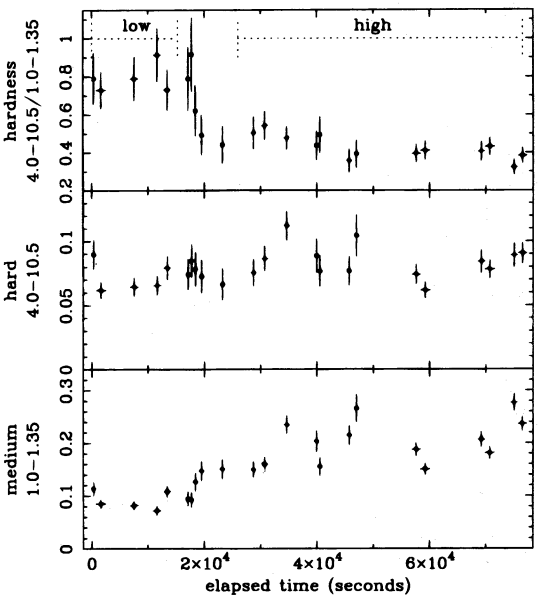

FIG. 4a

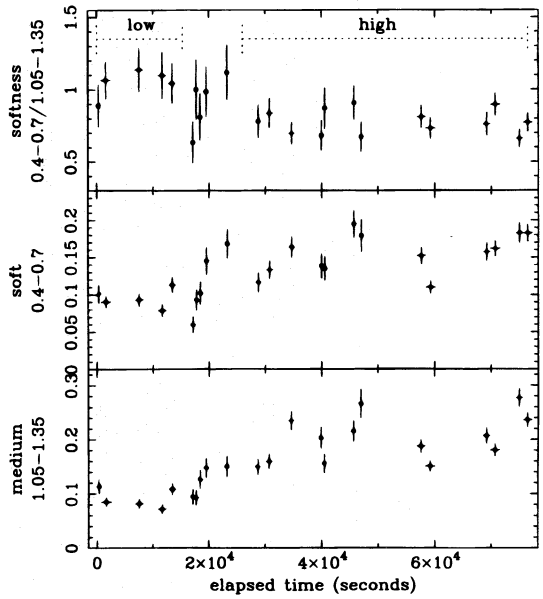

FIG. 4b

FIG. 4.—*ASCA* flux ratios as a function of elapsed time are shown in the upper panels, while the light curves in each energy band are shown in the lower panels. In both cases, the light curves were computed using variable bin size corresponding to good time intervals longer than 300 s (Ptak et al. 1994). The data accumulated in the high- and low-flux spectra are also marked. (*a*) The hardness ratio (4.0–10.5 keV/1.0–1.35 keV); (*b*) the softness ratio (0.4–0.7 keV/1.0–1.35 keV).

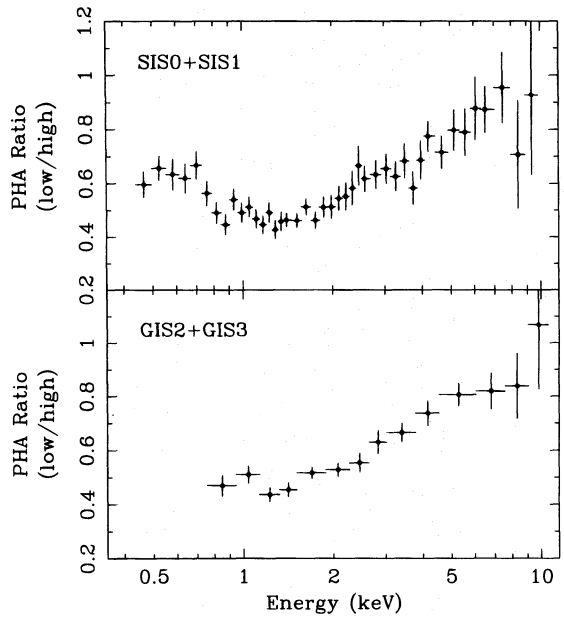

FIG. 5.—Pulse-height analyzer channel ratios of the low-state vs. high-state spectra. The upper and lower panels show the results from SIS0+SIS1 and GIS2+GIS3 spectra, respectively. These ratios confirm the variance analysis results shown in Fig. 2 that the spectrum is most variable at around 1 keV, less variable toward higher and lower energies, and essentially constant at around 10 keV. Further, the smoothly increasing ratios from 2 to 10 keV suggest that a variable photon index causes the spectral variability between these energies.

tainties are determined assuming 90% confidence and one parameter of interest ($\Delta\chi^2 = 2.71$).

4.2. *The Soft X-Ray Spectrum*

The shape of the soft X-ray spectrum can be seen by fixing the power-law indices to the values found above 2 keV, including the Galactic absorption (1.77×10^{20} cm^{-2}; Elvis, Wilkes, & Lockman 1989) and plotting the ratio of the data to the model. These plots are shown in Figures 6*a* and 6*b* for the SIS0 and GIS2 low-state and high-state spectra, respectively. In the low state, there is excess emission below 0.8 keV, which suggests the presence of a soft excess component (see, e.g., Mihara et al. 1994). In the high state, there is a deficit between 0.8 and 1.3 keV, which suggests the presence of a partially ionized absorber (see, e.g., Fabian et al. 1994). It is clear that an absorbed power law plus narrow iron line cannot model the spectra. Spectral fitting results of the SIS0:GIS2 and SIS1:GIS3 pairs are listed in Table 3 for low and high states separately. The iron line is discussed separately in § 4.5, and fit results are given in Table 4.

The soft excess component and warm absorber can be simply parameterized using a blackbody model and an absorption edge, respectively. The results from adding each of these components separately are given in the second and third panels of Table 3. Addition of either model component significantly improved the fits of both the low- and high-flux spectra. However, the addition of the blackbody improved the fit more than the edge in the low-flux case, while the reverse was true for the high-flux case, as expected from the residuals shown in Figure 6.

The fourth panel of Table 3 lists results from fitting with a model including both a blackbody and an edge. These fit results confirm the importance of the blackbody component in the low-state spectra and the edge in the high-state spectra. The blackbody temperatures and edge energies of the low- and high-state spectra are consistent. The edge energy near 0.74 keV is consistent with an origin of transmission through a partially ionized absorber dominated by O VII. The power-law slope of the low-flux spectra remains significantly flatter than that of the high-flux spectra ($\Delta\Gamma \sim 0.35$).

Next, to simulate the warm absorber better, a two-edge plus power-law model was tried, and the results are listed in the fifth panel of Table 3. The power-law indices are steep in both the low and high state, and the implied change in index is much smaller ($\Delta\chi^2 \sim 0.1$). This model has the same number of degrees of freedom as the power-law plus blackbody and edge model, but the fit is much poorer for the low-flux spectra ($\Delta\chi^2$ of 24 and 50 for the SIS0:GIS2 and SIS1:GIS3 pairs, respectively). In contrast, the fits of the high-flux spectra are improved somewhat by the additional edge ($\Delta\chi^2$ of 9 and 11). Addition of a blackbody component, while not necessary for the high-flux spectra, greatly improves the fit of the low-flux spectra ($\Delta\chi^2$ of 28 and 52) and results in a decrease in the low-flux photon index and an increase in the implied index change ($\Delta\Gamma \sim 0.35$). The temperature of the blackbody component in the low and high states is consistent at $kT \sim 120$ eV, although the limits on the temperature in the high state cannot be determined well for the SIS1:GIS3 pair. The edge energies near 0.74 and 0.87 keV found in the high state are approximately consistent with absorption by O VII and O VIII. In the low state, the O VII edge is clearly detected, but the second edge is not necessary. This suggests that the ionization of the gas in the high state is higher than in the low state.

We also modeled the warm absorber using a table model (see, e.g., Yaqoob, Warwick, & Pounds 1989). The model used here assumes that the power law is the sole source of ionizing photons. The density of the gas was assumed to be $10^{9.5}$ cm^{-3}. An analytic approximation based on a large number of CLOUDY runs was used to model the temperature as a function of ionization parameter. It was found to range between $\sim 5 \times 10^4$ K and $\sim 10 \times 10^4$ K. The advantages of using the warm absorber table model compared with the two-edge model are that there are two fewer parameters, and the parameters [log (U) and log (N_w)] can be directly interpreted. The disadvantage is that we must assume a particular model for the ionizing spectrum and gas. Further, in this model, only absorption is considered, and the emission lines expected if the warm absorber has a large covering factor are ignored (see, e.g., Netzer 1993). However, this model is sufficient for a general discussion given the statistical quality of these data (but see § 4.3.1).

The four groups of spectra were first fitted with a power-law plus warm absorber model (Table 3). As was found using the two-edge model, the fits of the high-flux spectra are acceptable, but the fits of the low-flux spectra are unacceptable. Addition of a blackbody component substantially improves the fit of the low-flux spectra, as shown in the eighth panel of Table 3, but it is not necessary to model the high-flux spectra. The ionized column density is consistent between the low- and high-flux states at log (N_w) ~ 21.8, while the ionization state log (U) is lower for the low-flux spectra (-0.78) compared to the high-flux spectra (-0.4). In this model, ionization states log (U) below and above ~ -0.4 are dominated by O VII and O VIII absorption, respectively. In contrast with the two-edge description of

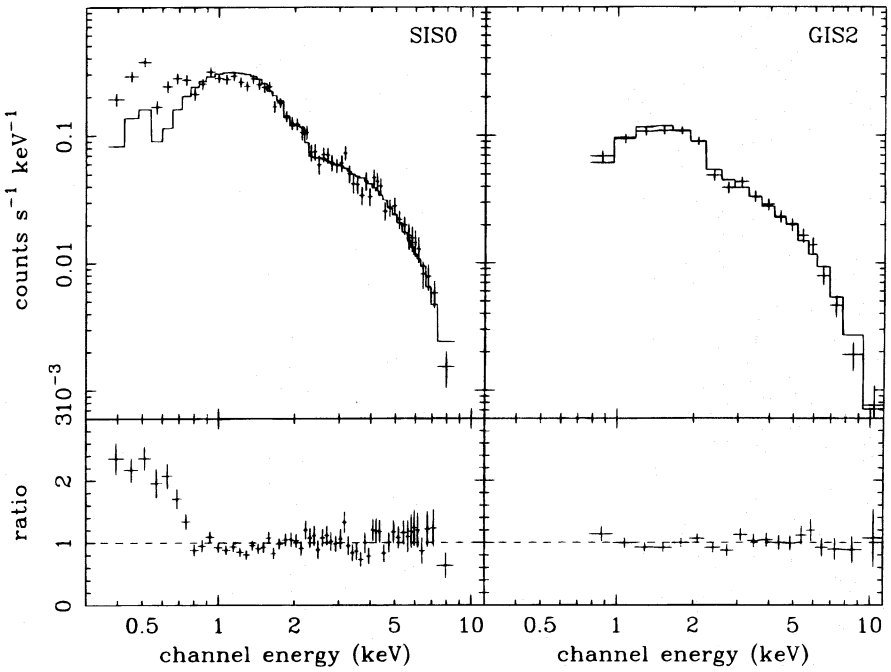

FIG. 6a

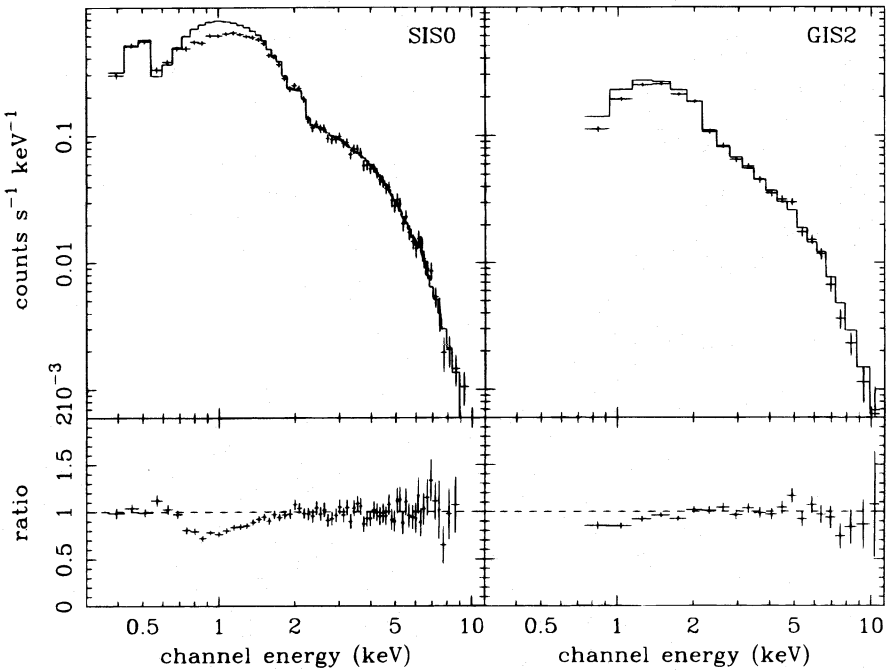

FIG. 6b

FIG. 6.—Residuals from a power-law fit above 2 keV for the SIS0:GIS2 pair accounting for Galactic absorption. (*a*) In the low state, the index is flat ($\Gamma = 1.56$), and excess emission is found below 0.8 keV, suggesting a soft excess component. (*b*) In the high state, the index is steep ($\Gamma = 2.01$), and a deficit is found around 0.8 keV, suggesting an ionized absorber.

the warm absorber, the use of the warm absorber table model resulted in a higher blackbody temperature in the high-flux state; however, the blackbody was barely detected in the high-flux spectra ($\Delta\chi^2$ of 4 and 5). Thus, the temperature of the soft component is model dependent, but the necessity of this component to model the low-flux spectra is not. The table model description of the warm absorber results in a slightly steeper index compared with the two-edge description. This is because the table model properly treats the absorption by gas with cosmic abundances (i.e., not only oxygen) producing curvature in the model between 1.5 and 2.5 keV. Thus, the value of the indices is slightly model dependent, but the change in index between the low and high states is not.

In summary, these results show that to model the high- and low-flux spectra consistently, both a soft excess com-

TABLE 3

ASCA SPECTRAL FITTING RESULTS

PARAMETER	LOW STATE		HIGH STATE	
	SIS0:GIS2	SIS1:GIS3	SIS0:GIS2	SIS1:GIS3
Power-Law Model:				
$N_H(\times 10^{21}$ cm$^{-2})$.....	Gal < 0.19	Gal < 0.20	Gal < 0.19	Gal < 0.192
Index	1.65 ± 0.04	$1.64^{+0.04}_{-0.05}$	1.92 ± 0.02	$1.91^{+0.01}_{-0.02}$
χ^2/d.o.f.	422/270	341/254	819/598	765/597
Power-Law plus Blackbody Model:				
$N_H(\times 10^{21}$ cm$^{-2})$.....	$0.84^{+0.51}_{-0.48}$	$0.75^{+0.53}_{-0.49}$	$0.95^{+0.22}_{-0.20}$	$1.02^{+0.22}_{-0.20}$
Index	$1.54^{+0.06}_{-0.07}$	$1.54^{+0.08}_{-0.07}$	1.96 ± 0.03	$1.98^{+0.04}_{-0.03}$
SIS PL norm[a]	$3.0^{+0.3}_{-0.2}$	$3.0^{+0.3}_{-0.2}$	7.7 ± 0.03	7.9 ± 0.03
kT (eV)	88^{+8}_{-6}	87^{+9}_{-7}	77^{+5}_{-4}	72 ± 5
SIS bb norm[b]	$2.5^{+2.1}_{-1.2}$	$2.3^{+2.1}_{-1.2}$	$4.2^{+1.5}_{-1.3}$	$5.4^{+2.0}_{-1.7}$
χ^2/d.o.f.	245/268	208/254	681/596	647/595
Power-Law plus Edge Model:				
$N_H(\times 10^{21}$ cm$^{-2})$.....	Gal < 0.18	Gal < 0.20	Gal < 0.26	Gal < 0.23
Index	1.87 ± 0.04	$1.83^{+0.06}_{-0.05}$	2.01 ± 0.02	$2.01^{+0.03}_{-0.02}$
SIS PL norm[a]	4.38 ± 0.18	$4.23^{+0.24}_{-0.23}$	$8.06^{+0.17}_{-0.15}$	$8.06^{+0.23}_{-0.17}$
Edge energy (keV).....	0.81 ± 0.02	$0.82^{+0.02}_{-0.03}$	$0.78^{+0.01}_{-0.03}$	0.75 ± 0.02
τ.....	1.01 ± 0.15	$0.89^{+0.21}_{-0.19}$	$0.49^{+0.07}_{-0.06}$	0.53 ± 0.70
χ^2/d.o.f.	344/268	279/254	651/596	608/595
Power-Law, Blackbody, and Edge Model:				
$N_H(\times 10^{21}$ cm$^{-2})$.....	Gal < 0.28 < 0.91	Gal < 0.42 < 0.88	$0.43^{+0.18}_{-0.20}$	Gal < 0.35 < 0.63
Index	$1.55^{+0.09}_{-0.05}$	1.57 ± 0.07	$1.99^{+0.02}_{-0.04}$	$2.00^{+0.04}_{-0.03}$
SIS PL norm[a]	$3.1^{+0.3}_{-0.2}$	3.2 ± 0.30	$7.9^{+0.2}_{-0.3}$	$8.0^{+0.4}_{-0.3}$
Edge energy (keV).....	$0.76^{+0.03}_{-0.04}$	0.74 ± 0.02	$0.74^{+0.03}_{-0.02}$	$0.75^{+0.02}_{-0.03}$
τ.....	$0.60^{+0.28}_{-0.25}$	$0.77^{+0.28}_{-0.30}$	$0.43^{+0.09}_{-0.10}$	$0.46^{+0.12}_{-0.11}$
kT (eV)	117 ± 18	121^{+21}_{-16}	101^{+19}_{-13}	91^{+48}_{-35}
SIS bb norm[b]	$0.95^{+1.19}_{-0.26}$	$1.12^{+0.82}_{-0.44}$	$0.81^{+0.56}_{-0.50}$	$0.54^{+1.04}_{-0.52}$
χ^2/d.o.f.	230/266	191/253	640/594	605/593
Power-Law and Two-Edge Model:				
$N_H(\times 10^{21}$ cm$^{-2})$.....	Gal < 0.22	Gal < 0.22	1.1 < 2.8	2.5 < 3.4
Index	$1.91^{+0.05}_{-0.04}$	1.90 ± 0.05	$2.02^{+0.05}_{-0.01}$	2.05 ± 0.04
SIS PL norm[a]	5.0 ± 0.20	4.9 ± 0.30	$8.2^{+0.5}_{-0.2}$	$8.5^{+0.5}_{-0.4}$
Edge energy (keV).....	$0.78^{+0.01}_{-0.02}$	0.77 ± 0.03	$0.74^{+0.02}_{-0.04}$	0.73 ± 0.02
τ.....	$1.00^{+0.18}_{-0.15}$	$1.01^{+0.23}_{-0.18}$	$0.43^{+0.08}_{-0.19}$	$0.51^{+0.09}_{-0.07}$
Edge energy (keV).....	$1.19^{+0.05}_{-0.03}$	$1.24^{+0.07}_{-0.14}$	$0.94^{+0.06}_{-0.24}$	$0.98^{+0.05}_{-0.04}$
τ.....	0.55 ± 0.11	$0.49^{+0.15}_{-0.11}$	$0.16^{+0.15}_{-0.06}$	$0.14^{+0.07}_{-0.06}$
χ^2/d.o.f.	254/266	241/252	631/594	594/593
Power-Law, Two-Edge, and Blackbody Model:				
$N_H(\times 10^{21}$ cm$^{-2})$.....	Gal < 0.32 < 0.81	Gal < 0.70	Gal < 0.29 < 0.44	Gal < 0.49 < 0.52
Index	$1.64^{+0.10}_{-0.09}$	1.62 ± 0.09	2.01 ± 0.04	2.05 ± 0.04
SIS PL norm[a]	$3.5^{+0.5}_{-0.4}$	$3.4^{+0.4}_{-0.3}$	8.2 ± 0.4	$8.5^{+0.5}_{-0.4}$
Edge energy (keV).....	0.76 ± 0.03	$0.75^{+0.02}_{-0.03}$	$0.73^{+0.02}_{-0.04}$	0.73 ± 0.02
τ.....	$0.67^{+0.26}_{-0.27}$	$0.84^{+0.37}_{-0.30}$	$0.40^{+0.15}_{-0.16}$	$0.51^{+0.08}_{-0.07}$
kT (eV)	115 ± 21	134^{+31}_{-33}	126^{+34}_{-29}	84[c]
SIS bb norm[b]	$0.88^{+1.00}_{-0.37}$	$0.69^{+1.04}_{-0.13}$	$0.29^{+0.31}_{-0.26}$	0 < 0.08
Edge energy (keV).....	$1.20^{+0.07}_{-0.17}$	1.104[c]	$0.87^{+0.12}_{-0.06}$	$0.98^{+0.05}_{-0.04}$
τ.....	$0.18^{+0.16}_{-0.14}$	0 < 0.16 < 0.27	$0.18^{+0.14}_{-0.09}$	0.14 ± 0.07
χ^2/d.o.f.	226/264	189/250	629/592	594/591

TABLE 3—*Continued*

Parameter	Low State		High State	
	SIS0:GIS2	SIS1:GIS3	SIS0:GIS2	SIS1:GIS3
Warm Absorber Model:				
$N_H(\times 10^{21}$ cm$^{-2})$	Gal < 0.18	Gal < 0.18	Gal < 0.23 < 0.30	$0.26^{+0.09}_{-0.08}$
Index	$2.05^{+0.04}_{-0.07}$	1.98 ± 0.08	$2.12^{+0.05}_{-0.04}$	$2.13^{+0.05}_{-0.04}$
SIS pl norm[a]	$6.4^{+0.5}_{-0.7}$	$5.7^{+0.5}_{-0.3}$	9.7 ± 0.5	9.9 ± 0.6
log (U)	$-0.17^{+0.08}_{-0.19}$	$-0.28^{+0.06}_{-0.09}$	$-0.38^{+0.05}_{-0.06}$	$-0.43^{+0.08}_{-0.06}$
log (N_w)[c]	$22.27^{+0.09}_{-0.17}$	22.13 ± 0.09	21.71 ± 0.07	$21.68^{+0.08}_{-0.06}$
χ^2/d.o.f.	294/268	269/254	634/596	601/595
Warm Absorber plus Blackbody Model:				
$N_H(\times 10^{21}$ cm$^{-2})$	Gal < 0.48 < 0.94	Gal < 0.36 < 0.79	Gal < 0.29 < 0.42	Gal < 0.23 < 0.40
Index	$1.70^{+0.13}_{-0.11}$	$1.70^{+0.14}_{-0.10}$	$2.12^{+0.05}_{-0.07}$	$2.10^{+0.07}_{-0.06}$
SIS PL norm[a]	$3.9^{+1.0}_{-0.6}$	$4.0^{+1.1}_{-0.6}$	$9.8^{+0.9}_{-0.8}$	$9.5^{+1.0}_{-0.6}$
log (U)	$-0.78^{+0.21}_{-0.32}$	$-0.79^{+0.25}_{-0.26}$	$-0.41^{+0.08}_{-0.07}$	$-0.42^{+0.06}_{-0.05}$
log (N_w)[d]	$21.78^{+0.36}_{-0.39}$	$21.84^{+0.40}_{-0.36}$	$21.82^{+0.13}_{-0.20}$	21.83 ± 0.11
kT (eV)	119^{+47}_{-18}	131^{+55}_{-24}	184^{+76}_{-103}	230^{+105}_{-57}
SIS bb norm[b]	$1.52^{+1.34}_{-0.66}$	$1.37^{+1.70}_{-0.48}$	$0.49^{+0.71}_{-0.46}$	$0.49^{+0.65}_{-0.44}$
χ^2/d.o.f.	234/266	194/253	630/594	596/593
Power-Law, Two-Edge, and Reflection Model:				
$N_H(\times 10^{21}$ cm$^{-2})$	Gal < 0.39	Gal < 0.50	Gal < 0.23 < 0.37	Gal < 0.28 < 0.44
Index	$2.05^{+0.12}_{-0.06}$	$2.04^{+0.17}_{-0.06}$	$2.06^{+0.08}_{-0.05}$	$2.07^{+0.09}_{-0.06}$
SIS PL norm[a]	$4.87^{+0.52}_{-0.22}$	$4.75^{+0.83}_{-0.26}$	$8.40^{+0.61}_{-0.36}$	$8.65^{+0.58}_{-0.51}$
SIS Refl norm[a]	$2.73^{+1.83}_{-1.10}$	$2.56^{+2.42}_{-0.94}$	0.21 < 1.24	0.26 < 1.35
Refl. Ratio	$5.5^{+2.5}_{-2.1}$	$8.3^{+6.1}_{-2.6}$	0.4 < 1.5	0.3 < 1.5
Edge energy (keV)	$1.18^{+0.05}_{-0.1}$	$1.11^{+0.05}_{-0.06}$	$0.94^{+0.07}_{-0.11}$	0.99 ± 0.04
τ	$0.44^{+0.08}_{-0.12}$	$0.38^{+0.13}_{-0.12}$	$0.18^{+0.06}_{-0.08}$	0.15 ± 0.07
Edge energy (keV)	0.77 ± 0.02	0.75 ± 0.02	0.73 ± 0.02	$0.73^{+0.02}_{-0.01}$
τ	0.98 ± 0.17	$0.90^{+0.18}_{-0.17}$	$0.44^{+0.10}_{-0.20}$	0.53 ± 0.09
χ^2/d.o.f.	230/263	201/250	631/593	594/590

NOTE.—The value "Gal" for the absorption refers to the spectral fit lower limit set to the Galactic value, 1.77×10^{20} cm^{-2} (Elvis, Wilkes, & Lockman 1989).

[a] $\times 10^{-3}$ photons keV^{-1} cm^{-2}s^{-1}.

[b] $\times 10^{-4} L_{39}/D_{10}^2$, where L_{39} is the source luminosity in 10^{39} ergs s^{-1} and D_{10} is the distance to the source in 10^{10} kpc.

[c] Unconstrained.

[d] log of the ionized column in units of cm^{-2}.

ponent and a warm absorber are required. When both of these components are included in the spectrum, the low-flux spectral index is significantly flatter than the high-flux index ($\Delta\Gamma \sim 0.35$).

TABLE 4

IRON LINE FITTING RESULTS

Parameter	Low State	High State
Power-Law plus Narrow-Line Model:		
Index	1.57 ± 0.07	$2.00^{+0.03}_{-0.04}$
Line flux[a]	1.8 < 3.0	$2.3^{+1.0}_{-1.2}$
Line eq. width (eV)	100 < 170	110^{+40}_{-55}
χ^2/d.o.f.	204/252	793/758
Power-Law, Narrow-Line, and Reflection Model:		
Index	1.66 ± 0.07	$2.08^{+0.04}_{-0.03}$
Line flux[a]	1.1 < 2.6	$1.8^{+0.9}_{-1.0}$
Line eq. width (eV)	35 < 84	47 ± 25
χ^2/d.o.f.	204/252	793/758

[a] $\times 10^{-5}$photonscm^{-2}s^{-1} in the line.

4.3. *Other Models*

4.3.1. *Other Soft Excess Models*

The soft excess component in the low-flux spectra was modeled adequately with a blackbody (with a single edge, $\chi^2 = 230/266$ d.o.f. for the SIS0:GIS2 pair). For comparison, other soft excess models including Raymond-Smith (cosmic abundances), bremsstrahlung, disk blackbody, and power law were tried. The power-law plus soft component model alone did not fit the low-flux spectra well. The disk blackbody model fitted the best, with χ^2 of 247/268 d.o.f. Including an edge generally improved the fits, but the Raymond-Smith and the power-law models could not describe the low-flux spectra well (χ^2 of 277 and 259/266 d.o.f., respectively), while the bremsstrahlung and the disk blackbody models could (χ^2 of 234 and 231/266 d.o.f., respectively). A slightly higher temperature was found using these models ($kT = 200$ eV and $kT = 145$ eV) compared with the blackbody model ($kT = 117$ eV), but nearly consistent edge energy, edge depth, and photon index were found. The indices obtained were flat ($\Gamma = 1.57$ in both cases).

The warm absorber table model used thus far models only the absorption edges of various ionized species. Since the line emission expected from a physical warm absorber might appear as an excess emission component, we also tested models calculated using XSTAR, which include emission lines from the warm absorber (Kallman & Krolik 1993). Fitting the SIS0:GIS2 pair with a power law plus emission only from a physical warm absorber in the line of sight resulted in a better fit with χ^2 of 292/277 d.o.f. Including an edge, to simulate the absorption by a warm absorber, resulted in a χ^2 of 261/268 d.o.f. However, a significantly better fit was found when a blackbody was also included ($\chi^2 = 228/264$ d.o.f.), and the resulting power-law index was again flat ($\Gamma = 1.55$). Similarly, emission from reflection by a warm absorber could not alone describe the spectrum (alone: $\chi^2 = 299/268$ d.o.f.; with an edge: $\chi^2 = 268/266$ d.o.f.; with an edge and a blackbody: $\chi^2 = 227/264$ d.o.f.). In the final case, the index was flat ($\Gamma = 1.55$).

Soft excess emission can also be produced by reflection from an ionized disk (Ross & Fabian 1993; Zycki et al. 1994). We fitted the low-flux spectrum with an ionized disk table model computed according to Zycki et al. (1994). For power law plus disk emission only, the χ^2 was 262/269 d.o.f., but the ratio of the reflected flux to direct emission was 5.8. Since the ratio should be near 1 for the isotropic static case, we considered this result to be unphysical. Addition of an edge gave χ^2 of 248/267 d.o.f., but again the ratio was too large at 5.5. Addition of a blackbody gave $\chi^2 = 228/265$ d.o.f., with the ratio reduced to a physical value of $R = 1.23$ and a flat index $\Gamma = 1.61$.

These results show that soft excess models without line emission fit the spectra well, but we cannot distinguish among them, possibly because of the poor statistics due to the relatively short exposure in the low state and the decrease in sensitivity toward low energies of the *ASCA* SIS. Further, the flat spectral index obtained in the low state is robust against changes in the soft excess model.

4.3.2. *Partial Covering Models*

Another possible origin of soft emission is leakage through a partially covering absorber (e.g., NGC 4151: Weaver et al. 1994). The spectral variability would then result from a change in the covering fraction. However, the partial covering model does not fit the low-flux SIS0 and GIS2 spectra well ($\chi^2 = 298$ for 268 d.o.f.), the resulting power law is forced to be steep ($\Gamma = 2.42$), and both low- and high-energy residuals are seen. These can be modeled by reflection, in which case the fit is good ($\chi^2 = 225/263$ d.o.f.), but the power law is very steep ($\Gamma = 3.0$), and the ratio of the reflected emission to primary emission is required to be 20. This model is unphysical, so we conclude that partial covering cannot adequately model the soft excess component. Finally, a decrease in the fraction of the source covered can only produce a steepening of the spectrum with an increase in flux and cannot explain the hardening of the spectrum below 1 keV indicated by the softness ratio (Fig. 4*b*).

A scattering and dual absorber model was used to describe the complex X-ray spectrum of NGC 4151 (Weaver et al. 1994). For Mrk 766, this model does not give a good fit ($\chi^2 = 244/266$ d.o.f.), and the photon index is steep ($\Gamma = 2.84$). Low-energy residuals suggest an unmodeled absorption edge. When an edge is included, the fit is good ($\chi^2 = 222/264$ d.o.f.), but the power-law index is very steep ($\Gamma = 2.94$). Again, this steep index seems unphysical, so the dual absorber model is rejected.

5. REFLECTION

The spectral index change is robust against changes in models of the soft excess component and warm absorber because the low-flux spectrum is flat at high energies. The reflection spectrum is also flat (see, e.g., George & Fabian 1991) and could produce a hard tail if the reflection component normalization is high compared with the power-law normalization. This could be observed if the response of the reflection component lags variability of the incident X-rays and would be expected if the light-crossing timescale of the reflection region is long compared with the source variability timescale or if the reflection region is located far from the X-ray source (e.g., in the molecular torus; Ghisellini, Haardt, & Matt 1994; Krolik, Madau, & Zycki 1994; Leighly et al. 1996).

We define the reflection ratio to be 1 under the conditions that nonvarying primary power-law emission from an isotropic point source illuminates an infinite optically thick disk. In this case, the reflection spectral component is not important in the spectrum below 5 keV. Thus, we can estimate the contribution of the reflection by fitting the spectra below 5 keV and comparing with the fit results over the full range. A power-law plus two-edge fit of the SIS0:GIS2 spectra results in a steep photon index (low state: $\Gamma = 1.95$ and $\chi^2 = 214.4/230$ d.o.f., high state: $\Gamma = 2.02$ and $\chi^2 = 524/519$ d.o.f.). Addition of a blackbody component to the model improved the fit of the low-flux spectra and flattened the photon index ($\Gamma = 1.67$ and $\chi^2 = 197/228$ d.o.f.) but had no effect on the high-flux spectral fit. If the table model is used to model the warm absorber, similar results are obtained, although both indices are found to be slightly steeper. Thus, fitting below 5 keV shows that the index variability is still required and also that the measured low-energy index is consistent with the data above ~ 5 keV.

A reflection ratio much larger than 1 results in a flat spectrum toward high energies. Fitting the spectra with a power law plus two edges and reflection allowing the ratio to be free produces a good fit with a steep index that is consistent between the low- and high-flux spectra (Table 3). However, to explain the low-flux spectrum, the reflection ratio must be 5–8, while the high-flux spectra require a reflection ratio of only 0.5. Most importantly, the reflection component normalization is required to be significantly *higher* in the low-flux state compared with the high-flux state, so a reflection lag cannot explain the spectral variability. Further, such a large reflection ratio should be accompanied by a large equivalent width narrow iron line in the low-state spectrum, and such a line is not observed (§ 4.5).

The timing analysis results also rule out a lag in neutral reflection as the origin of the spectral variability. Since the neutral reflection spectrum flux decreases toward low energies, only spectral softening with an increase in power-law flux is predicted, whereas a hardening of the spectrum below 1 keV was observed. If the surface of the reflector is ionized, the opacity is reduced at low energies, and a soft X-ray reflection component plus emission lines should be observed (Ross & Fabian 1993; Zycki et al. 1994), which results in hardening of the low-flux spectrum with an increase in power-law flux. It was shown in § 4.3.1 that the ionized disk model does not produce a good fit alone, mostly because the soft excess does not show evidence for

line emission.

5.1. *The Iron Line*

The presence of the iron Kα line in Seyfert 1 nuclei spectra is well established (see, e.g., Nandra & Pounds 1994). Mrk 766 was not observed using *Ginga*, and an iron Kα line had not yet been observed in its spectrum. To look for the iron line, we fitted the spectra from all four detectors simultaneously above 2 keV. Because of the continuum spectral variability, the low- and high-state spectra were fitted separately. A power-law model resulted in χ^2/d.o.f. of 206/253 and 806/759 for the low and high states, respectively. Addition of a narrow ($\sigma = 0$ keV) redshifted line with the energy fixed at 6.4 keV gave the results presented in Table 4. There is no strong evidence for a narrow line with rest energy 6.4 keV in the low-flux spectra ($\Delta\chi^2 \sim 2$). In the high-flux spectra, $\Delta\chi^2$ is 13 corresponding to an F-statistic value of 12.4, which indicates the presence of a line with confidence greater than 99.9%. Thus, the presence of an iron emission line is confirmed in this source. The ratio of data to power-law model for the summed SIS0 and SIS1 spectra shows the narrow line and ionized iron edge (Fig. 7). The nondetection in the low-flux spectra can be explained by the poor statistics resulting from lower flux and shorter exposure. If the high-flux data are divided into several spectra characterized by shorter exposures, the presence of a line in the spectra from all detectors separately cannot be confirmed. Next, the line energy was allowed to be free. The high-state line energy is consistent with 6.4 keV, and a lower energy line is marginally detected in the low-state spectra. The line energy in both states is consistent with an origin in primarily neutral material, and emission from highly ionized material is excluded. The line equivalent width is $\sim$100 eV, consistent with that expected from emission from an accretion disk (see, e.g., George & Fabian 1991). Broad iron lines have been discovered in the *ASCA* spectra of several active galactic nuclei (AGNs) (see, e.g., Mushotzky et al. 1995). A broad line is preferred in the low-flux spectra, although the addition of another parameter reduces the χ^2 by only 5, so again the detection is marginal. The line is narrow in the high-flux spectra, constrained with $\sigma < 0.2$ keV. The shape of the high-energy continuum changes the measured line parameters. When reflection with ratio fixed to 1 is included, similar results were obtained as before, but the measured equivalent widths were smaller (Table 4).

These results also support the hypothesis that a lag in the reflection component cannot be the origin of the spectral variability. A lag implies that the bulk of the reflected emission should come from a substantial distance from the source, and so the line would be expected to be narrow.

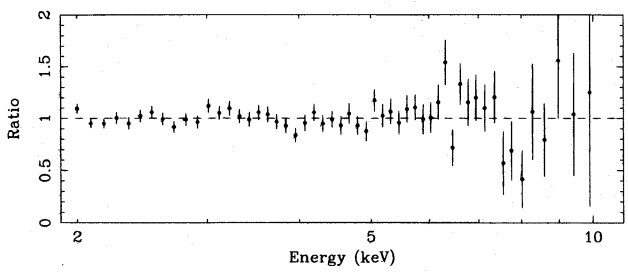

FIG. 7.—Ratio of data to model for a power-law fit to the summed SIS0 and SIS1 data above 2 keV showing the narrow iron line and ionized iron absorption edge.

However, the large reflection ratio required to fit the low-flux spectra predicts a very large equivalent width ($> \sim$500 eV) narrow line, which would be easily detected if present.

5.2. *Quantifying the Spectral Variability*

The results of the previous sections indicate that the power-law with blackbody and warm absorber model provides the best fit to both the low- and high-flux spectra. A change in spectral index seems to be indicated. However, since the model is complex, spectra from the two states must be fitted simultaneously to determine which parameters necessarily change. Neutral absorption, originating in our Galaxy and the host galaxy, was assumed not to change, and the iron line was modeled as narrow with fixed energy. Combined fits were done using both descriptions of the warm absorber.

When two edges were used to model the warm absorber, the edge energies were equated in the high- and low-state models. This was done because the low-state spectra could not constrain the higher edge energy, and since the edges are identified as O VII and O VIII edges, no change is expected in the energies. This model fitted the low and high spectra well (χ^2 of 860.1/859 d.o.f. and 789.8/844 d.o.f. for the SIS0:GIS2 and SIS1:GIS3 spectra, respectively). The temperatures of the blackbody were consistent between the low and high states, so these were equated, which resulted in a negligible increase in χ^2. No other parameters could be equated without resulting in a large change in χ^2. The results are listed in the top panel of Table 5, and they indicate that a significant change in index and blackbody normalization occurred. The edge energies are roughly consistent with absorption by O VII and O VIII. The optical depths of these edges are consistent between the low and high state, so no change in the ionization of the warm absorber can be determined from these fits. However, the best-fit value of $\tau_{\rm O\ VII}$ is larger in the low state than in the high state, and the reverse is approximately true for $\tau_{\rm O\ VIII}$. This suggests that an increase in the ionization occurred, but the statistics are too poor to require this conclusion.

The results of the combined fits using the warm absorber table model are listed in the second panel of Table 5. The ionized column densities were consistent, so they were equated in the spectral fitting. As noted previously, when the warm absorber was described using the table model, the blackbody temperature was found to be higher in the high state than in the low state (Table 3). When the temperatures are equated in the combined fits, the increase in χ^2 is 2.7 and 5.7 for the SIS0:GIS2 and SIS1:GIS3, respectively, significant with 90% and 97.5% confidence. However, this effect is clearly model dependent and may be due to the shape of the warm absorber model and possibly the absence of emission lines in the model, and thus the implied blackbody temperature change is probably not physical. Three parameters changed between the low and high states: the power-law index, the blackbody normalization, and the ionization parameter. As these parameters are coupled in the spectral fitting, to evaluate the significance of the change, the χ^2 contours were plotted for each pair of parameters (Figs. 8*a*, 8*b*, and 8*c*). These show that the results are consistent between the SIS0:GIS2 and SIS1:GIS3 spectral pairs and that the index change, the ionization state change, and the blackbody normalization change are significant with >99%, 90%, and 68% confidence, respectively. We note that the change in the ionization state is a model-dependent

TABLE 5

COMBINED SPECTRAL FITS

PARAMETER	SIS0:GIS2 Low State	SIS0:GIS2 High State	SIS1:GIS3 Low State	SIS1:GIS3 High State
Two-Edge Model:				
$N_H(\times 10^{21}$ cm$^{-2})$.....	Gal < 0.27 < 0.45		Gal < 0.25 < 0.37	
Index	1.58 ± 0.08	2.02 ± 0.04	$1.60^{+0.08}_{-0.07}$	2.05 ± 0.04
SIS PL norm[a]	3.2 ± 0.30	$8.3^{+0.4}_{-0.3}$	3.2 ± 0.3	8.6 ± 0.4
kT (eV)	123^{+22}_{-17}		133^{+26}_{-21}	
SIS BB norm[b]	$0.89^{+0.34}_{-0.22}$	0.19 < 0.61	$0.84^{+0.24}_{-0.16}$	0 < 0.23
Edge energy (keV).....	$0.73^{+0.03}_{-0.01}$		$0.74^{+0.01}_{-0.02}$	
τ.....	$0.66^{+0.28}_{-0.25}$	$0.47^{+0.08}_{-0.09}$	$0.83^{+0.19}_{-0.17}$	$0.52^{+0.07}_{-0.08}$
Edge energy (keV).....	$0.97^{+0.05}_{-0.16}$		0.99 ± 0.04	
τ.....	0.11 < 0.30	$0.15^{+0.06}_{-0.08}$	0.13 < 0.30	$0.14^{+0.07}_{-0.06}$
χ^2/d.o.f	860.1/860		790.7/845	
Warm Absorber Model:				
$N_H(\times 10^{21}$ cm$^{-2})$.....	$0.33^{+0.16}_{-0.15}$		$0.30^{+0.17}_{-0.10}$	
Index	$1.66^{+0.07}_{-0.06}$	$2.12^{+0.05}_{-0.04}$	$1.67^{+0.07}_{-0.06}$	$2.14^{+0.05}_{-0.04}$
SIS PL norm[a]	$3.7^{+0.2}_{-0.3}$	9.8 ± 0.6	$3.6^{+0.3}_{-0.2}$	10.0 ± 0.6
kT (eV)	117^{+13}_{-14}		121^{+12}_{-14}	
SIS BB norm[b]	$1.34^{+0.43}_{-0.38}$	0.42 < 0.97	$1.20^{+0.49}_{-0.28}$	0.02 < 0.52
log (N_w)[c]	$21.68^{+0.04}_{-0.08}$		21.69 ± 0.08	
log (U).....	$-0.85^{+0.16}_{-0.15}$	-0.42 ± 0.08	$-0.87^{+0.16}_{-0.15}$	$-0.42^{+0.07}_{-0.09}$
χ^2/d.o.f	867.1/863		801.8/848	

NOTE.—The value "Gal" for the absorption refers to the spectral fit lower limit set to the Galactic value, 1.77×10^{20} cm^{-2} (Elvis, Wilkes & Lockman 1989).

[a] $\times 10^{-3}$ photons keV^{-1} cm^{-2}s^{-1}.

[b] $\times 10^{-4} L_{39}/D_{10}^2$, where L_{39} is the source luminosity in 10^{39} ergs s^{-1} and D_{10} is the distance to the source in 10^{10} kpc.

[c] log of the ionized column in units of cm^{-2}.

result, as we cannot demonstrate a change in the optical depths of the two oxygen edges. Figures 9*a* and 9*b* show the best-fitting models, spectra, and ratios between spectra and model for the low and high state SIS0:GIS2 spectra. Figure 10 shows the best-fit models for the low- and high-state SIS0 spectra. Note that the pivot point for the power-law change is ~9 keV.

5.3. *ROSAT* Spectral Fitting

The *ASCA* data show that the soft X-ray spectrum is complex, comprised of a power law with variable index, a warm absorber with variable ionization state, and a blackbody with marginally variable normalization and model-dependent temperature. Seven parameters are required to describe the spectrum in the *ROSAT* band. Because of the poor spectral resolution, the PSPC spectra have five independent channels. Thus, detailed fitting of the PSPC spectra is of limited value, as multiple models are acceptable. Qualitatively, the spectra from the 1992 and 1993 observations are very soft and cannot be adequately modeled using a single power law plus absorption. A soft component like a blackbody gives a good fit, with $kT \sim 70$–90 eV and a power law with index ~1.9–2.0. An edge can also model the spectrum, but the spectral index is steeper at ~2.5.

6. DISCUSSION

6.1. *The Hard Spectral Variability*

The most significant result of this study was the observation of dramatic photon index variability from ~1.6 to ~2.0, over several thousand seconds and confined to a single event. We discuss this result in light of current models of the X-ray power-law emission in AGN.

6.1.1. *General Considerations*

The high-energy power law observed from AGNs can be successfully and plausibly explained by inverse-Comptonization by high-energy electrons of soft UV photons likely originating in the accretion disk. The rapid X-ray variability of some AGNs implies a high radiation density in the nucleus that results in production of electron-positron pairs. The importance of pair production is determined by the compactness parameter,

$$l = L\sigma_T / R m_e c^3 , \quad (1)$$

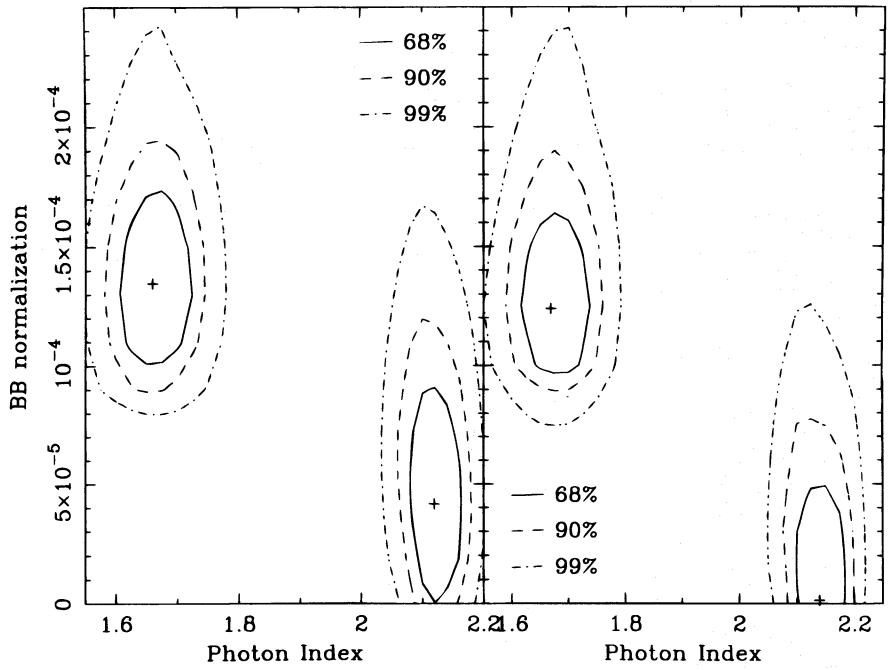

FIG. 8a

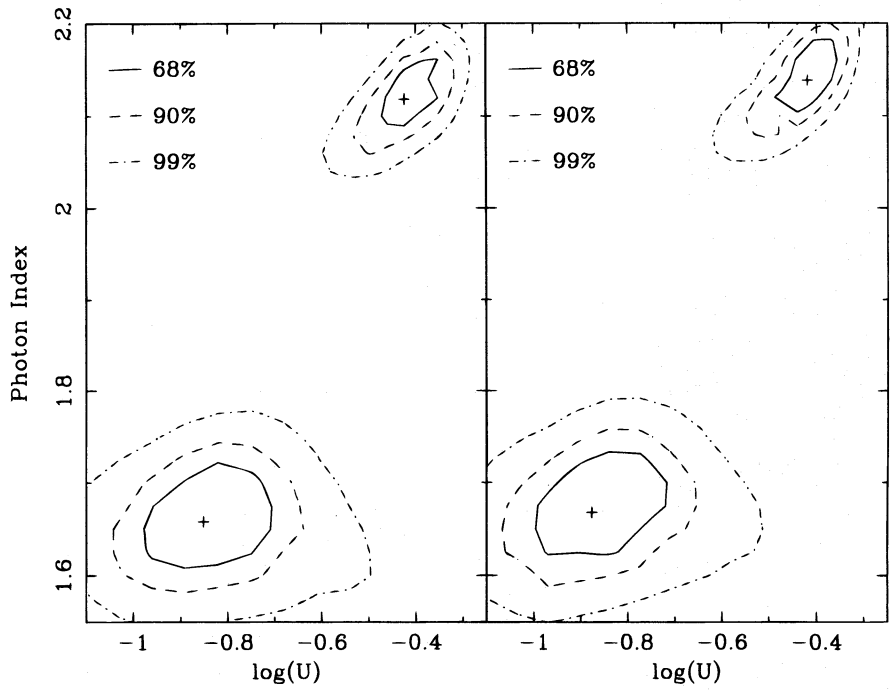

FIG. 8b

FIG. 8.—χ^2 contours for 2 degrees of freedom for the combined power-law, blackbody, and warm absorber model fits. The SIS0:GIS2 and SIS1:GIS3 contours are shown on the left and right sides, respectively. (*a*) Photon index vs. blackbody normalization, (*b*) log (U) vs. photon index, and (*c*) log (U) vs. blackbody normalization. The change in the photon index is significant at >99% confidence, the change in the ionization parameter is significant at 90% confidence, and the change in the blackbody normalization is significant at 68% confidence.

where L is the luminosity, R is the source size, σ_T is the Thompson scattering cross section, m_e is the mass of the electron, and c is the speed of light. If the compactness is high, the optical depth to pair production will exceed unity, and pairs will be produced that can substantially modify the emerging spectrum. Generally speaking, these models can be differentiated by whether the high-energy electrons are thermal or accelerated by nonthermal processes, since pair production limits the highest energy attainable in the thermal plasma. In rapidly variable AGNs, however, both thermal and nonthermal processes may be present (Ghisellini et al. 1993).

The results presented here suggest that Mrk 766 is compact enough that pairs should be produced in the nucleus. The X-ray flux was observed to change by a factor of 2 in ~1000 s. This corresponds to a source size upper

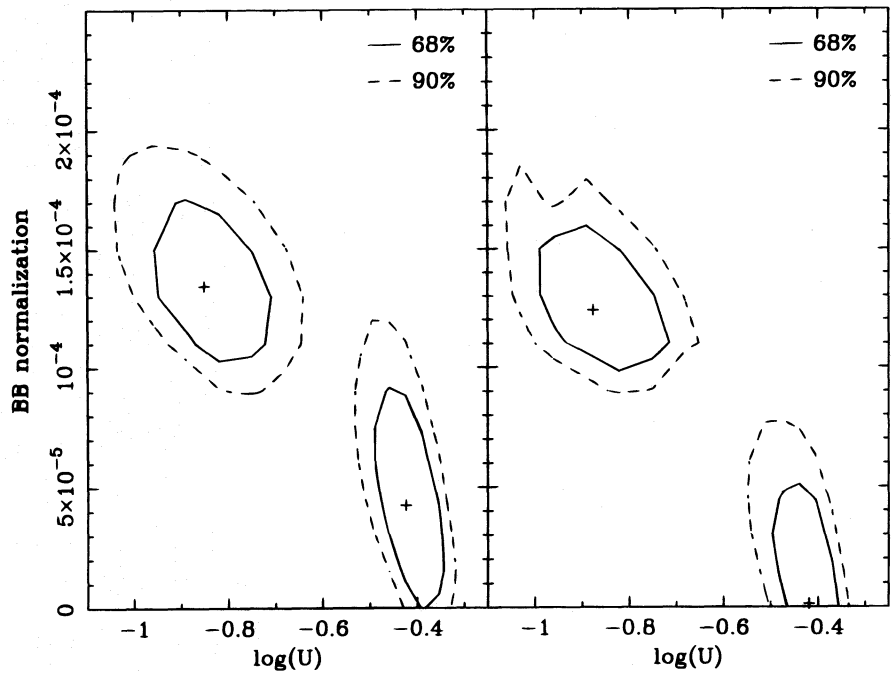

FIG. 8c

limit of $R < c\Delta t \sim 3 \times 10^{13}$ cm. The 2–10 keV luminosity is 1.3×10^{43} ergs s^{-1} in the high state, which implies an X-ray compactness parameter of $l_X \sim 12$. The hard compactness parameter, proportional to the total luminosity in the hard component, could be substantially larger. If the compactness parameters are larger than 10, pair production should be important if there are an adequate number of γ-ray photons present. In nonthermal models, the γ-rays are produced through upscattering of soft photons by extremely relativistic electrons. In thermal models, the origin is primarily the high-energy tail of the thermal spectrum, and thus the number of γ-rays depends on the temperature of the plasma. OSSE observations of a few AGNs find that the temperature is large enough that electron positron pairs should be produced (e.g., see Fig. 1 of Fabian 1994); however, there have been no high-energy spectra obtained from Mrk 766.

6.1.2. *Simple Thermal Comptonization Models*

If the source does not contain many pairs and if the power-law results from unsaturated Comptonization of soft photons, the spectral parameters are very simply related to one another (see, e.g., Rybicki & Lightman 1979). The slope of the power law depends inversely on the Compton y-parameter, which is proportional to a power of the temperature, so an increase in temperature implies a decrease in index. However, if the soft photon input is constant, the pivot point energy of the photon index change should be the energy of the soft input photons. In contrast, we observe the pivot point to be much higher, at $\sim$9 keV.

If the thermal plasma is pair dominated, Ghisellini & Haardt (1994) show that there is a one-to-one mapping of the observables (kT and α, where $\alpha = \Gamma - 1$ is the energy index) to the plasma parameters (l_H and l_H/l_S, where l_H and l_S are the hard and soft compactnesses, characteristic of the relativistic electrons and the soft [UV] seed photons, respectively). Our observed increase in photon index by $\Delta\alpha \sim 0.4$ implies a decrease in l_H/l_S by a factor of 10 (Fig. 2 of Ghisellini & Haardt 1994). We observed a 2–10 keV flux increase by a factor of 1.3, but since the power-law pivot point is $\sim$9 keV, integration to high energies may show that the low-flux state luminosity is actually larger than the high-flux state luminosity. OSSE observations of several Seyfert 1 galaxies have found that the power spectrum is cut off above several hundred keV (see, e.g., Fabian 1994). Integration of the power law from 2 keV to the generous upper limit of 500 keV shows that the low state l_H is at most a factor of 2 larger than the high-state l_H, predicting an increase in index by only $\sim$0.1. Further, the timescale of the spectral variability, less than 10,000 s, precludes a large increase in l_S, since this short timescale would be the order of the orbital period at the innermost stable orbit for a $< 5 \times 10^7 M_\odot$ black hole. A change in the accretion rate should be characterized by the viscous or radial drift timescale, estimated by Molendi & Maccacaro (1994) to be 2.6 days. Further, the *ROSAT* spectral variability can be most naturally explained by a constant (on timescales of 1 day) soft component dominating the softest X-ray band (see § 5.2). Finally, as Ghisellini & Haardt (1994) note, if reprocessing in the disk is important, l_H/l_S would be expected to remain approximately constant, and little intrinsic index variability should be observed. However, this model is very simple, and predictions may change substantially if a realistic geometry or self-consistent treatment of the two phases is considered.

6.1.3. *Nonthermal Comptonization Models*

Static nonthermal models of X-ray emission have been investigated by several authors (see, e.g., Svensson 1994 and references therein), and 2–10 keV spectral index variability has been studied by Yaqoob (1992). Most simply and generally, soft photons with dimensionless frequency x_S and compactness l_S are scattered by relativistic electrons with Lorentz factor γ_0 and compactness l_H. First order scattering

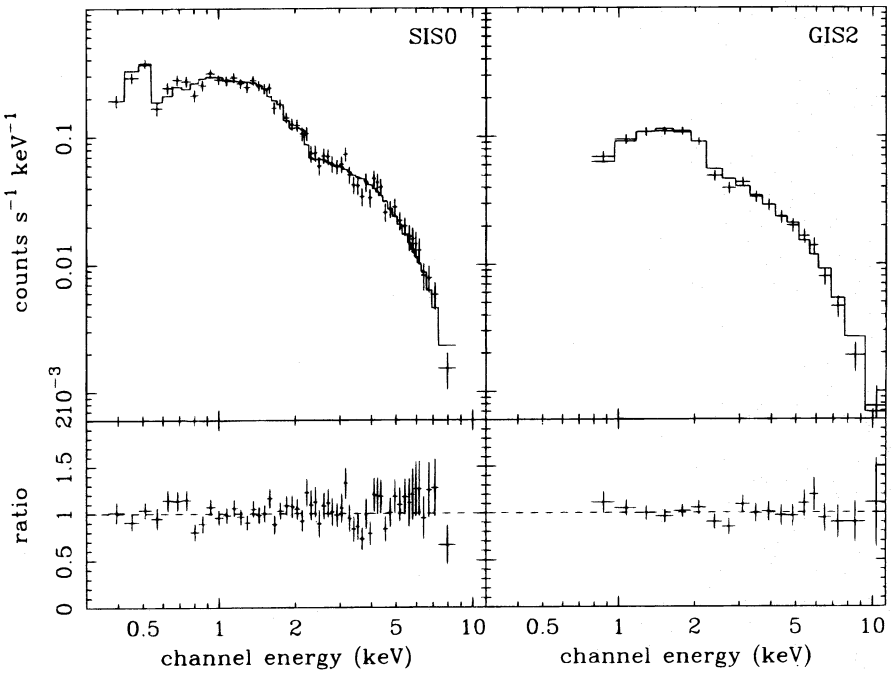

FIG. 9*a*

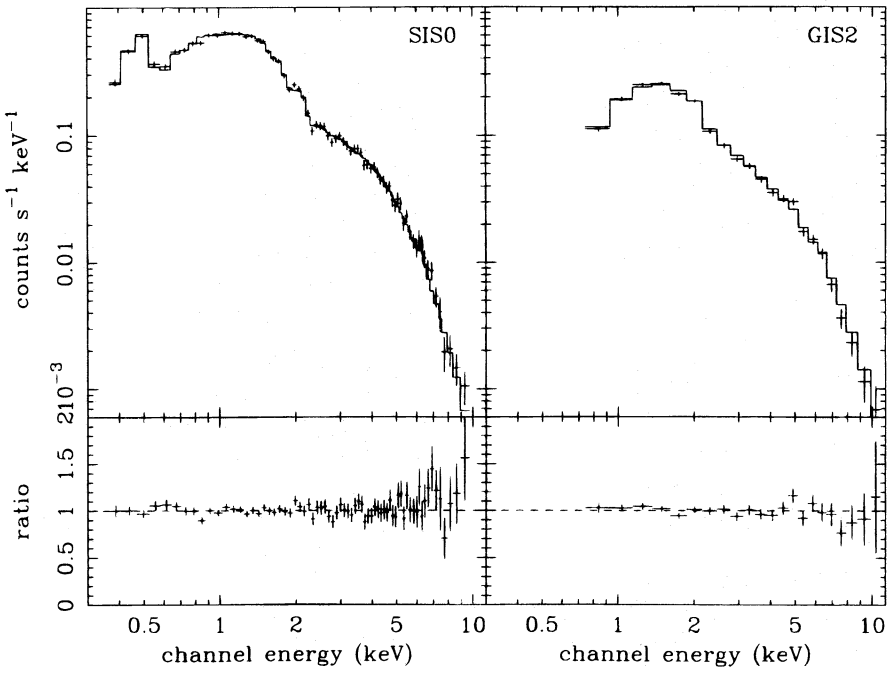

FIG. 9*b*

FIG. 9.—Best-fit model (power-law, blackbody, and warm absorber table), spectra, and ratio of spectra to model for the SIS0:GIS2 pair, on the left and right sides, respectively. (*a*) The low state; (*b*) the high state.

produces a flat photon spectrum with $\Gamma \sim 1.5$ extending to $x_{\max,1} = \max(4/3\gamma_0^2 x_s, \gamma_0)$ (Svensson 1987). Pairs are produced if the photon spectrum extends to sufficiently high energies and if the optical depth to pair production is greater than unity. Soft photons reprocessed by pairs have a steeper spectrum with $\Gamma = 1.75$ breaking sharply at $x_B = 2\gamma_0^4(2/3x_s)^3$. If the energy of pair-reprocessed photons is relatively low, they could be observed as an X-ray soft excess. If the energy of reprocessed photons is high enough, additional pair generations will be produced, which will result in a pair cascade. In that case, the photon spectrum is steep with Γ approaching 2 (see, e.g., Svensson 1987).

A nonthermal model can naturally explain the observed change in index, the disappearance of the soft excess component, and the confinement of the spectral variability to a single event. The photon index variability could result from a transition from a first-order pair spectrum to a cascade caused by a sudden increase in the Lorentz factor of the

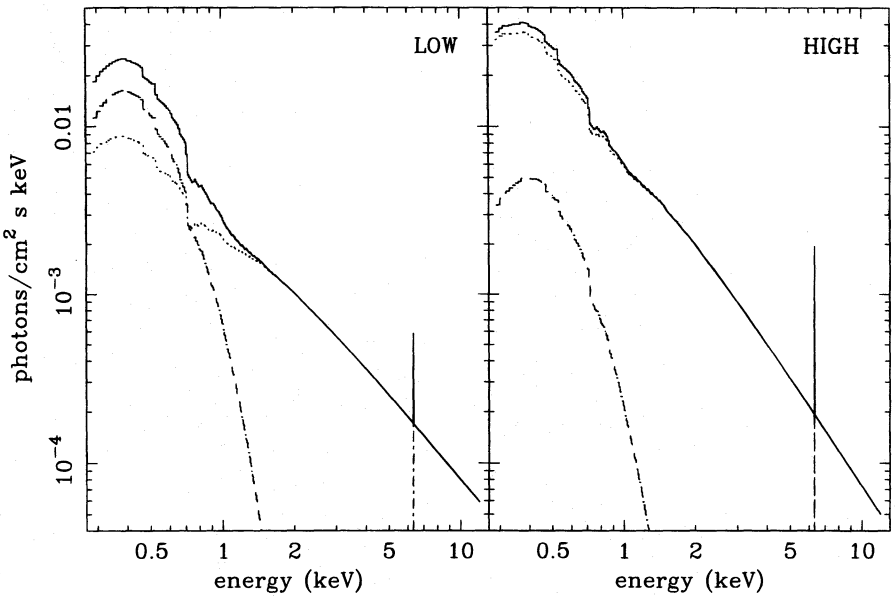

FIG. 10.—Unfolded best-fit model (power-law, blackbody, and warm absorber table) showing additive model components for the SIS. The low-state and high-state models are shown on the left and right sides, respectively. Note the pivot point for the variable power-law index occurs near 9 keV and that the large decrease in blackbody normalization is marginally significant (see Fig. 6).

relativistic electrons. Thus, the low-flux spectrum is comprised of the inverse-Compton cooling spectrum, characterized by the hard X-ray power law with photon index near 1.5, and the first-order optically thin pair-reprocessed spectrum, observed as the soft excess component. The high-flux spectrum is comprised of a pair cascade spectrum, characterized by the hard X-ray power law with photon index near 2. The soft excess component disappears in the high-flux spectrum as the maximum energy of the pair-reprocessed spectrum increases far beyond the observed X-ray band, which results in the cascade. The change in flux in the X-ray band depends on the change of hard compactness l_H that can be expected to accompany the change in Lorentz factor, and flux variability uncorrelated with spectral variability would occur through variation in l_H alone.

A possible difficulty with nonthermal models that produce flat spectra is that, in general, they overpredict the gamma-ray background. However, recent work shows that if the nonthermal plasma is in a corona above a disk, γ-ray photons are more efficiently depleted, and, depending on the compactness, a strong spectral cutoff below 200 keV is predicted (Tritz 1990; Tsuruta & Kellen 1995).

6.2. *The Soft Spectral Variability*

The *ROSAT* spectrum was observed to become harder as the flux increased, consistent with the lower amplitude variability observed at softest energies. A most natural explanation for this behavior is variability between the relative normalizations of the power-law and soft excess component. This would be observed if the flux of the soft component were nearly constant on the timescale of an observation. In terms of current physical models, it could imply that the soft component is dominated by primary emission from an accretion disk and reprocessed hard emission is relatively less important. The fraction of blackbody flux in the softest band can be estimated by comparing the relative variability of the hardest band where the power law dominates with the relative variability of the softest band where the soft component dominates. This scenario predicts that if a static soft excess component comprises a large fraction of the flux in the softest band, any flux change must be accompanied by a hardness ratio change, while if the blackbody comprises only a small fraction of the flux, variability in hard and soft bands should be correlated.

Overall, the *ROSAT* PSPC data are qualitatively consistent with this scenario. In the 1992 observation, the spectrum was harder at high flux and correlated variability was observed, while at low flux, uncorrelated variability was found. In the 1991 observation, when the flux was lower and the spectrum generally softer, only uncorrelated variability was observed. This scenario can also explain the lack of spectral variability seen in the *ROSAT* All Sky Survey data (Molendi et al. 1993) since at that time the source was bright and power-law emission may have dominated the soft component emission. Qualitatively and on short timescales, there are difficulties with this scenario. In 1992, the hardest and softest bands decrease by 50% and 25%, respectively, overall, which implies that the soft component must contribute the same percentages of the soft band flux in the high and low states, respectively. However, at high flux, there is a dip in flux by 30% just after the start of the observation, and no change in the softness ratio was observed. Similarly, at low flux, there is an increase by 30% in the hard band approximately 6×10^4s after the start of the observation, but no change in the soft band emission was observed. In combination, these two results cannot be explained if the blackbody flux is constant and no other parameters change. Reprocessing, neglected so far, may be able to explain large-amplitude correlated variability at high flux.

Other models cannot explain the observed spectral variability. Netzer et al. (1994) showed that variability of the warm absorber in response to ionizing flux changes could not explain the spectral variability found during the 1992 observation. In general, if the soft component were dominated by reprocessing, the soft X-ray variability would be expected to track the hard component variability. However, substantial spectral variability of the incident continuum could result in some spectral variability of the reprocessed

component. Changes in the accretion rate (Molendi & Maccacaro 1994) cannot explain the orbit-to-orbit spectral variability as the predicted timescales are much longer.

6.3. *The Change in the Warm Absorber*

In the *ASCA* spectra, we found that there was no evidence that the ionized absorption column density changed between the high state and the low state; however, we found that the ionization parameter changed with 90% confidence. This result is model dependent, as we could not demonstrate that the optical depth of the oxygen edges changed significantly.

The best-fit ionization parameter log (U) changed from ~ -0.85 in the low state to ~ -0.42 in the high state, implying an increase in flux of ionizing photons by a factor of 2.7. It is interesting that this is quite close to the implied change in flux by a factor of 3.1 of the intrinsic power law at 0.7 keV. The observed photon index variability implies a larger change in the flux of ionizing photons, assuming the power law extends to low energies. The spectral changes occurred over a timescale of several thousand seconds. The recombination timescale for O VIII is about $2 \times 10^{11} T_e^{0.5} n^{-1}$ s (see, e.g., Turner et al. 1993) or about 5.5 hr using the parameters assumed in this model (or longer if the gas is rarer). Thus, the gas may not be in photoionization equilibrium in the high-flux state, and the larger population of O VIII implied by the increase in the ionization parameter may result from ions that are directly stripped of an electron by the increased number of photons with energy near 0.7 keV. Further observations are necessary to determine the response of the ionized material to a decrease in flux since a change in ionization would be observed only if recombination had occurred.

A change in the ionization correlated with an increase in flux has not been previously reported from *ASCA* data. An increase in column density and no change in ionization accompanied an increase in flux in MCG -6-30-15 (Fabian et al. 1994). Explaining the spectral variability during an increase in flux by a change in warm absorber properties in NGC 3227 required a decrease in ionization and an increase in column (Ptak et al. 1994). In another observation of MCG -6-30-15, an increase in the optical depth of the O VIII edge during a flux decrease was interpreted as evidence for recombination of O IX (Otani 1995).

6.4. *Hard X-Ray Emission from Narrow-Line Seyfert 1s*

The soft X-ray properties of narrow-line Seyfert 1s are well studied (Boller et al. 1996), but few hard X-ray observations have been reported. The *ASCA* observation of Mrk 766 represents one of the first observations of the hard emission from these objects.

We found a hard power law with variable photon index in Mrk 766 and the spectral variability that was not strictly flux correlated. Similar photon index variability that was flux correlated has been discovered from NGC 4051 (Guainazzi et al. 1996), a Seyfert 1 galaxy that shares many properties with NLS1s. In contrast, a very steep spectrum with photon index ~ 2.6, a dominant soft excess and no variability was observed from the narrow-line Seyfert 1 RE 1034+39 (Pounds et al. 1995). Because these spectral and variability properties are similar to those characteristic of black hole candidates in the high state (see, e.g., Nowak 1991), it was postulated that RE 1034+39 represents a Seyfert 1 galaxy in the high state (Pounds et al. 1995).

The marked differences between the hard X-ray properties of Mrk 766 and RE 1034+39 are interesting. Black hole candidates in the low state are characterized by a flat hard X-ray power law and more rapid, larger amplitude hard X-ray variability (see, e.g., Nowak 1995). These properties more closely resemble the observational results from Mrk 766 and NGC 4051 than do the properties of black hole candidates in the high state. Further observations of NLS1s may find that the spectral and variability properties fall into two classes: those with steep hard X-ray spectra, dominant soft X-ray emission, and lower amplitude short-term hard X-ray variability, and those with flat hard X-ray spectra, less soft X-ray emission, and rapid hard X-ray variability. There is perhaps already some evidence for such a division. While many NLS1s are very bright soft X-ray objects commonly found in soft X-ray samples, relatively few have hard X-ray detections by *HEAO 1* A-2.

Further support for this scenario may come if repeated X-ray observations discover that some objects have made the transition between two states. This could have been what had occurred in objects observed to have varied by factors of 10 or more between two *ROSAT* observations (e.g. Zwicky 159.034, Brandt et al. 1995; WPVS007, Grupe et al. 1995). Well-studied broad-line Seyfert 1 galaxies are not observed to undergo this kind of transition. The fact that many well-studied AGNs are hard X-ray–selected while NLS1s are clearly soft X-ray–selected objects further supports this hypothesis.

In black hole candidates, it is widely believed that the high state is characterized by a relatively larger accretion rate compared with the low state. Thus, the behavior of NLS1s may result from a relatively larger accretion rate. If the processes fueling AGNs are common for Seyferts, a relatively larger accretion rate would be observed in systems with relatively small black hole masses.

7. CONCLUSIONS

We report analysis of *ASCA* and *ROSAT* observations of the narrow-line Seyfert 1 galaxy Mrk 766. In the *ASCA* observation, rapid variability with doubling timescale of order ~ 1000 s was observed, and dramatic spectral variability over a time period of less than $\sim 10{,}000$s was discovered. Confined to a single event, during a 2–10 keV flux increase, the spectrum above and below ~ 1 keV softened and hardened, respectively. The low- and high-flux spectra could be described with a model consisting of a power law, iron line, warm absorber, and soft excess modeled as a blackbody. The spectral variability was a result of a highly significant increase in the intrinsic power-law index from ~ 1.6 to ~ 2.0 with the pivot point at ~ 9 keV, a model-dependent increase in the ionization of the warm absorber, and a marginal decrease in the soft excess component. A 100 eV equivalent width narrow iron line was detected in the high-flux spectrum but not in the low-flux spectrum, most likely because of poor statistics. Variability on timescales as short as ~ 2400 s was found in the *ROSAT* data. Because the variability in the softest *ROSAT* band, below 0.4 keV, had relatively lower amplitude than the harder bands, spectral hardening during flux increases was detected on timescales as short as the orbital period of ~ 6000s.

The spectral index change, the disappearance of the soft component in the *ASCA* band, and the confinement of the spectral variability to a single event could be naturally

explained in terms of nonthermal Comptonization models. We postulate that the index change occurred through a transition from a first-order pair-reprocessed spectrum to a pair cascade spectrum brought about by a sudden increase in the Lorentz factor of the injected relativistic electrons. The first-order pair-reprocessed spectrum observed in the low state as a soft excess disappeared in the high-state cascade spectrum. Variations in the hard compactness resulted in pure flux variability. The measured increase in the warm absorber ionization corresponds to the increase in flux near the oxygen edges that results from the power-law index change. The spectral variability in the *ROSAT* data was most naturally explained by a variable hard component and a nonvariable soft component that dominated the softest band and may be primary emission from an accretion disk, which perhaps implies that reprocessing is relatively less important in this object.

The flat and variable hard power-law index observed in Mrk 766 is similar to that observed in NGC 4051 (Guainazzi et al. 1996), a Seyfert 1 with many properties common to NLS1s, but contrasts markedly with the very steep hard X-ray index $\Gamma \sim 2.6$ found in the NLS1 object RE 1034+39 (Pounds et al. 1995). Further hard X-ray observations of NLS1s using *ASCA* are necessary to understand clearly the hard X-ray properties of these sources.

This research has made use of data obtained through the High Energy Astrophysics Science Archive Research Center Online Service, provided by the NASA-Goddard Space Flight Center. The authors thank T. Kallman and P. Zycki for the use of their spectral table models. K. M. L. acknowledges receipt of a National Research Council fellowship at NASA/GSFC and a Japanese Science and Technology Agency fellowship at RIKEN and useful conversations with M. Cappi. K. M. L. acknowledges support by a *ROSAT* AO4 Guest Observer grant and an *ASCA* AO1 Guest Observer grant.

REFERENCES

Boller, Th., Brandt, W. N., & Fink, H. 1996, A&A, 305, 53
Brandt, W. N., Fabian, A. C., Nandra, K., & Tsuruta, S. 1993, MNRAS, 255, 996
Brandt, W. N., Pounds, K. A., & Fink, H. 1995, MNRAS, 273, 47
Done, C., Madejski, G. M., Mushotzky, R. F., Turner, T. J., Koyama, K., & Kunieda, H., 1992, ApJ, 400, 138
Edelson, R. 1992, ApJ, 401, 516
Elvis, M., Wilkes, B. J., & Lockman, F. J. 1989, AJ, 97, 777
Fabian, A. C. 1994, ApJS, 92, 555
Fabian, A. C., et al. 1994, PASJ, 46, L59
George, I. M., & Fabian, A. C. 1991, MNRAS, 249, 352
Ghisellini, G., & Haardt, F. 1994, ApJ, 429, L53
Ghisellini, G., Haardt, F., & Fabian, A. C. 1993, MNRAS, 263, L9
Ghisellini, G., Haardt, F., & Matt, G. 1994, MNRAS, 267, 743
Goodrich, R. W. 1989, ApJ, 342, 224
Grupe, D., Beuermann, K., Mannheim, K., Thomas, H.-C., Fink, H. H., & de Martino, D. 1995, A&A, 300, L21
Guainazzi, M., et al. 1996, PASJ, in press
Kallman, T., & Krolik, J. H. 1993, GSFC preprint
Krolik, J. H., Madau, P., & Zycki, P. T. 1994, ApJ, 420, 57
Leighly, K. M., Kunieda, H., Awaki, H., & Tsuruta, S. 1996, ApJ, 463, 158
Mihara, T., Matsuoka, M., Mushotzky, R. F., Kunieda, K., Otani, C., Miyamoto, S., & Yamauchi, M. 1994, PASJ 46, L137
Molendi, S., & Maccacaro, T. 1994, A&A, 291, 420
Molendi, S., Maccacaro, T., & Schaeidt, S. 1993, A&A, 271, 18
Mushotzky, R. F., et al. 1995, MNRAS, 272, L9
Nandra, K., & Pounds, K. A. 1994, MNRAS, 268, 405
Netzer, H. 1993, ApJ, 411, 594
Netzer, H., Turner, T. J., & George, I. M. 1994, ApJ, 435, 106
Nowak, M. A. 1995, PASP, 107, 55
Osterbrock, D. E., & Pogge, R. W. 1985, ApJ, 297, 166
Otani, C. 1995, Ph.D. thesis, Tokyo Univ.
Pounds, K. A., Done, C., & Osborne, J. P. 1995, MNRAS, 277, 5P
Ptak, A., Yaqoob, T., Serlemitsos, P. J., Mushotzky, R., & Otani, C. 1994, ApJ, 436, L31
Ross, R. R., & Fabian, A. C. 1993, MNRAS, 261, 74
Rybicki, G. B., & Lightman, A. P. 1979, Radiative Processes in Astrophysics (New York: Wiley)
Svensson, R. 1987, MNRAS, 227, 403
———. 1994, ApJS, 92, 585
Tritz, B. 1990, Ph.D. thesis, Montana State Univ.
Tsuruta, S., & Kellen, M. 1995, ApJ, 453, 9
Turner, T. J., Nandra, K., George, I. M., Fabian, A. C., & Pounds, K. A. 1993, ApJ, 419, 127
Urry, C. M., et al. 1989, in Proc. 23rd ESLAB Symp., ed. J. Hunt & B. Battrick (Paris: ESA), 789
Weaver, K. A., Yaqoob, T., Holt, S. S., Mushotzky, R. F., Matsuoka, M., & Yamauchi, M. 1994, ApJ, 436, L27
Yaqoob, T. 1992, MNRAS, 258, 198
Yaqoob, T., Warwick, R. S., & Pounds, K. A. 1989, MNRAS, 236, 153
Zycki, P. T., Krolik, J. H., Zdziarski, A. J., & Kallman, T. R. 1994, ApJ, 437, 597